SELF-ASSEMBLY TECHNIQUE FOR PRODUCING L-ARGININE/HYDROXYAPATITE COATINGS ON Ti6Al4V IMPLANTS

by

Ilayda Duru

BSc, Chemistry, Yıldız Technical University, 2013

Submitted to the Institute of Biomedical Engineering
in partial fulfillment of the requirements
for the degree of
Master of Science
in
Biomedical Engineering

Boğaziçi University
2017

ACKNOWLEDGMENTS

First, I would like to express my sincere appreciation and special thanks to my advisor Assist. Prof. Dr. Duygu Ege for her precious guidance, encouragement and inspire during my research. I also want to thank to committee members for my thesis defense, Prof. Dr. Albert Güveniş and Assist. Prof. Dr. Selim Coşkun.

I would like to express my gratitude to Assist. Prof. Dr. Mücahit Yılmaz and his MSc student Ayşe Karataş in Necmettin Erbakan University for their valuable support on sputtering studies and hospitality. I also would like to give special thanks to Dr. Ceren Yılmaz Akkaya, Dr. Amir Motallebzadeh and Dr. M. Barış Yağcı in Surface Science and Technology Center in Koç University for their great help and support on many analyses and processes of my research.

I want to thank to my family, especially my precious mother who's always been there for me. I also would like to thank to all my best friends who always support me and believe in me during my work. Finally, I want to thank to my laboratory colleagues for their help and support during my research.

ACADEMIC ETHICS AND INTEGRITY STATEMENT

I, Ilayda Duru, hereby certify that I am aware of the Academic Ethics and Integrity Policy issued by the Council of Higher Education (YÖK) and I fully acknowledge all the consequences due to its violation by plagiarism or any other way.

Name :

Signature:

Date:

ABSTRACT

SELF-ASSEMBLY TECHNIQUE FOR PRODUCING L-ARGININE/HYDROXYAPATITE COATINGS ON Ti6Al4V IMPLANTS

In the present study, we introduce a self-assembly method to produce L-arginine (L-Arg)/Hydroxyapatite (HA) coatings. Firstly, Ti6Al4V substrates were etched in a concentrated solution of HCl/H_2SO_4. ZrO_2 was reactively sputtered on Ti6Al4V as an intermediate layer between HA and Ti6Al4V. Reactive magnetron sputtering was performed at 200 W and 200 °C for 4 hours. HA was deposited on ZrO_2 layer by electrophoretic deposition (EPD) at 30 V in 205 seconds. HA suspension was obtained by ultrasonic and magnetic agitation of 1 g HA in 35 ml isopropanol for 3 hours. Finally, the samples were immersed in L-Arg solution in phosphate buffered saline (pH=7.4) and incubated at room temperature for 24 hours. Scanning Electron Microscopy (SEM), X-Ray Diffractometry (XRD), Fourier Transform Infrared Spectroscopy (FTIR), Raman and X-Ray Photoelectron Spectroscopy (XPS) analyses were performed to characterize the coated and uncoated Ti6Al4V implants. Raman and XRD spectra of ZrO_2 layer demonstrated the characteristic peaks of monoclinic structure. The most characteristic bands on Raman spectrum were a doublet at 181 and 189 cm^{-1}, a broad peak at 477 cm^{-1}. Moreover, XRD spectrum revealed that ZrO_2 coating had a monoclinic crystal structure. FTIR and C1s spectra spectra of L-Arg/HA coating revealed the formation of new bonds which were C-O/N and protonated O-C=O. According to XPS analyses, C/Ca ratio increased with the addition of L-Arg and Ca/P ratio was decreased. It can be concluded that L-Arg particles were self-assembled on HA layer by binding of the carboxyl group of L-Arg to calcium atoms of HA. Overall, L-Arg/HA coatings were successfully coated on ZrO_2-coated Ti6Al4V orthopedic implants by self-assembly method.

Keywords: Self-assembly, amino acid, orthopedic implant.

ÖZET

Ti6Al4V İMPLANTLAR ÜZERİNDE KENDİLİĞİNDEN YIĞILMA TEKNİĞİ İLE L-ARJİNİN/HİDROKSİAPATİT KAPLAMALAR ÜRETME

Bu çalışmada, kendiliğinden yığılma yöntemi ile L-Arjinin (L-Arg)/ Hidroksiapatit (HA) kaplamalar üretildi. ŻrO_2, HA ve Ti6Al4V arasında bir orta katman olarak reaktif magnetron sıçratma yöntemiyle Ti6Al4V üzerine kaplandı. Reaktif magnetron sıçratma işlemi, 200 W ve 200 °C' de 4 saat boyunca yapıldı. ZrO_2 tabakası üzerine elektroforetik kaplama yöntemi kullanılarak 30 V' ta 205 saniye boyunca HA kaplandı. Elektroforetik kaplama için 1 g HA' in 35 ml izopropanol içerisinde ultrasonik banyo ve magnetik karıştırıcı ile karıştırılmasıyla HA süspansiyonu hazırlandı. Daha sonra örnekler, L-Arg' ın PBS çözeltisi (pH=7.4) içerisine yerleştirildi ve oda sıcaklığında 24 saat boyunca inkübe edildi. Kaplanmış ve kaplanmamış Ti6Al4V implantların karakterizasyonu Taramalı Elektron Mikroskobu (SEM), X Işını Kırınımı (XRD), Fourier Dönüşümlü Infrared Spektroskopisi (FTIR), Raman ve X-Ray Fotoelektron Spektroskopisi (XPS) ile gerçekleştirildi. ZrO_2 kaplamanın XRD ve Raman analizleri, monoklinik yapının karakteristik piklerini gösterdi. Raman spektrumundaki en karakteristik pikler 181 ve 189 cm^{-1}' deki dublet pik ve 477 cm^{-1}' deki geniş piktir. Ayrıca XRD analizi, ZrO_2 kaplamanın monoklinik fazdan oluşan tek fazlı yapıya sahip olduğunu açığa çıkarmıştır. L-Arg/HA kaplamanın FTIR ve XPS spektrumları, C-O/N bağını ve protonlanmış karboksil grubunu gösterdi. XPS analizlerine göre, L-Arg eklenmesiyle birlikte C/Ca oranı artmış ve Ca/P oranı azalmıştır. Özetle; L-Arg, kendi karboksil grubu ile HA tabakasının kalsiyumu arasında bağ oluşturarak HA tabakasının üzerinde kendiliğinden yığıldı. Sonuç olarak; kendiliğinden yığılma yöntemi kullanılarak, ZrO_2 kaplı Ti6Al4V ortopedik implantlar üzerinde L-Arg/HA kaplamalar başarıyla oluşturuldu.

Anahtar Sözcükler: Kendiliğinden yığılma, amino asit, ortopedik implant

TABLE OF CONTENTS

ACKNOWLEDGMENTS . . . iii
ACADEMIC ETHICS AND INTEGRITY STATEMENT . . . iv
ABSTRACT . . . v
ÖZET . . . vi
LIST OF FIGURES . . . ix
LIST OF TABLES . . . xi
LIST OF ABBREVIATIONS . . . xii
1. INTRODUCTION . . . 1
1.1 Motivation . . . 1
1.2 Objectives . . . 3
1.3 Outline . . . 3
2. BACKGROUND . . . 4
2.1 Bone . . . 4
2.1.1 Bone and Joint Diseases . . . 6
2.2 Total Hip Arthroplasty (THA) and Total Knee Arthroplasty (TKA) . . . 9
2.2.1 Failure of THA and TKA . . . 9
2.3 Ti6Al4V for Orthopedic Implants . . . 10
2.4 Bioceramic Coatings . . . 11
2.4.1 Bioinert Ceramic Coatings . . . 11
2.4.1.1 ZrO_2 . . . 11
2.4.2 Bioactive Ceramic Coatings . . . 14
2.4.2.1 Hydroxyapatite . . . 14
2.5 Arg in Biomedical Studies . . . 17
3. MATERIALS AND METHODS . . . 20
3.1 Surface Treatment of Ti6Al4V Substrates . . . 20
3.2 Characterization of Etched Substrates . . . 21
3.2.1 Scanning Electron Microscopy (SEM) . . . 21
3.2.2 Stylus Profilometer . . . 21
3.3 Deposition of ZrO_2 by Reactive DC Magnetron Sputtering . . . 21

3.4 Characterization of ZrO_2 Coatings 23
3.4.1 SEM 23
3.4.2 Raman Spectroscopy 23
3.4.3 XRD 23
3.5 Production of HA Coatings by EPD 23
3.5.1 Preparation of HA Suspension 23
3.5.2 EPD 24
3.5.3 Sintering of HA Coatings 25
3.6 Functionalization of HA Layer with L-Arg 25
3.7 Characterization of HA and L-Arg/HA Coatings 25
3.7.1 SEM 25
3.7.2 FTIR 25
3.7.3 XPS 26
3.7.4 Ninhydrin Test 26
4. RESULTS 27
4.1 Surface Treatment of Ti6Al4V Substrates 27
4.2 ZrO_2 Coating 29
4.3 HA Coating 32
4.4 Functionalization of HA coating with L-Arg 34
5. DISCUSSION 38
5.1 Future Studies 42
APPENDIX A. SCAN ON XRD SOFTWARE 43
APPENDIX B. Subculturing 44
REFERENCES 45

LIST OF FIGURES

Figure 2.1	Structure of Bone [23]	4
Figure 2.2	(a) Osteoblast and osteoclast cell lineages (HSC: Hematopoietic stem cell, MP: Mesenchymal stem cell), (b) The differentiation processes of mesenchymal stem cells into osteoblasts [25]	6
Figure 2.3	Scanning electron micrographs of osteoporotic trabecular bone (Left) and normal trabecular bone (right) [29]	7
Figure 2.4	Hip osteoarthritis [32]	8
Figure 2.5	Total Hip Arthroplasty [42]	9
Figure 2.6	Zr-Nb (2.5% Nb) Femoral Head with a Thermally Oxidized Surface-Brand Name: Oxinium	12
Figure 2.7	Sputtering Process [71]	14
Figure 2.8	The Crystalline Structure of HA (Green, red, orange and white symbols represent Ca, O, P and H respectively)[76]	15
Figure 2.9	EPD Process [88]	17
Figure 2.10	Molecular Structure of L-Arg (drawn on ChemSketch)	17
Figure 3.1	Etchant solution after 4-hour-treatment	20
Figure 3.2	Ti6Al4V samples not coated (left) ZrO_2-coated (right)	22
Figure 3.3	Experimental setup for EPD	24
Figure 4.1	(a) Pristine (2000x, scale bar: 20 μm) and etched Ti6Al4V substrates in different magnifications (b) 2000x, scale bar: 20 μm (c) 10000x, scale bar: 20 μm (d) 50000x, scale bar: 1 μm	27
Figure 4.2	SEM images of ZrO_2 coating on etched substrates in magnifications of (a) 2000x, scale bar: 20 μm (b) 5000x, scale bar: 10 μm (c)10000x, scale bar: 5 μm (d) 20000x, scale bar: 2 μm	29
Figure 4.3	Raman spectrum of ZrO_2 coating	30
Figure 4.4	XRD spectrum of ZrO_2 coating (m: monoclinic, s: substrate)	31
Figure 4.5	SEM micrographs of HA coating in different magnifications (a) 50000x, scale bar: 1 μm (b) 100000x, scale bar: 500 nm	32
Figure 4.6	XRD spectrum of HA coating	33

Figure 4.7	SEM micrographs of L-Arg /HA coating in different magnifications (a) 50000x, scale bar: 1 μm (b) 100000x, scale bar: 500 nm	34
Figure 4.8	FTIR spectrums of HA and L-Arg/HA coatings	35
Figure 4.9	C1s spectrums of HA and L-Arg/HA coatings	36
Figure 4.10	(a) HA coating after ninhydrin test (b) L-Arg/HA coating after ninhydrin test	37
Figure A.1	Software scan of ZrO_2 coating (Blue lines: monoclinic phase, Green lines: substrate, Red lines: Undetected tetragonal phase)	43
Figure B.1	Confluent human bone marrow mesenchymal stem cells at passage 2	44

LIST OF TABLES

Table 3.1	Reactive sputtering parameters	22
Table 4.1	The R_a, R_q and R_z values of etched Ti6Al4V substrates	28
Table 4.2	Ca/P and C/Ca ratios of HA and L-Arg/HA coatings	37

LIST OF ABBREVIATIONS

HA	Hydroxyapatite
L-Arg	L-Arginine
SEM	Scanning Electron Microscopy
XRD	X-Ray Diffractometry
FTIR	Fourier Transform Infrared Spectroscopy
XPS	X-Ray Photoelectron Spectroscopy
EPD	Electrophoretic Deposition
THA	Total Hip Arthroplasty
TKA	Total Knee Arthroplasty

1. INTRODUCTION

1.1 Motivation

Ti6Al4V is extensively utilized in orthopedic and dental implants due to its high mechanical strength, corrosion resistance, toughness, low density and biocompatibility [1] - [5]. Smooth-surfaced Ti6Al4V exhibit osseointegration in dental applications. However, it is not adequate for osseointegration in load-bearing applications due to the intervention of the fibrous tissue [6]. Fibrous tissue encapsulates and isolates Ti6Al4V from surrounding bone after implantation [6, 7]. Therefore, it is essential to increase osseointegration ability of Ti6Al4V for orthopedic applications and developing bioactive surfaces on Ti6Al4V is of great interest in implant research [7].

Several methods have been reported in order to design a bioactive surface on titanium implants such as roughening the surface, coating with calcium phosphates and coating with biomolecules [8]. Calcium phosphates including HA are deposited on Ti6Al4V implants in order to induce bone ingrowth and bone-implant coating. However, the pre-osteogenic ability of calcium phosphates is generally insufficient for large bone defects. Therefore, incorporation of biologically active molecules to hydroxyapatite is needed in order to increase osseointegration since biologically active molecules can induce cellular activity and tissue responses [9, 10]. Biochemical modification utilizes critical organic components of bone [10]. Many molecules have been studied in calcium phosphate coatings. These molecules can be classified as amino acids [11, 12], extracellular matrix proteins [13], peptides [13, 14], and growth factors [8, 15]. Amino acids are of great interest since they are more stable molecules and less expensive, compared to peptides or proteins [16].

L-Arg has cationic charge in physiological conditions [17]. The cationic charge of L-Arg facilitate the protein binding of HA [18]. HA interacts with bovine serum albumin by the bond between Ca^{2+} and -COO^{-}. According to the study of Lee et al.

[18], Arg provides -NH^{3+} groups and increases the number of cationic groups on HA and these groups lead HA to bind -COO^{-} on bovine serum albumin. Moreover, Gonzalez-Mc Quire et al. [11] demonstrated high bioactivity of Arg/HA coating. After immersion in T-SBF for 5 days, an even calcium phosphate layer was formed on Arg/HA coated titanium. They also showed the self-repair property of Arg/HA coating after scratch test.

The cell culture studies with mesenchymal stem cells demonstrated the positive effect of arg on their proliferation at an early stage. Moreover, mRNA expression of osteogenic gene expression markers which are alkaline phosphatase, type Iα1 collagen and osteocalcin increased with the addition of arg. mRNA expression of transcription factors which are osterix, Runx2 and DIx5, key agents for stimulating osteoblast-specific gene expression, increased with the addition of arg. Arg also increased mRNA expression of osteogenic gene expression markers which are alkaline phosphatase, type Iα1 collagen and osteocalcin. According to Huh et al. [19], arg enhances osteoblastogenesis by regulating Wnt/β-catenin independent signaling and the mechanisms including NFATc that regulate MSC fate and differentiation. Vater et al. [12] also indicated that arg increased the adhesion, proliferation and ALP activity of bone marrow derived mesenchymal stem cells on calcium phosphate cements.

Overall, L-Arg has potential in order to enhance osseointegration of HA-coated orthopedic implants. This thesis introduces self-assembly method in order to functionalize HA coatings with L-Arg. Based on the results achieved so far, self-assembly is an efficient technique for synthesizing L-Arg/HA coatings.

1.2 Objectives

The aim of this study is to increase osseointegration of HA-coated Ti6Al4V implants. For this purpose, L-Arg was incorporated to HA coatings by self-assembly technique for the first time. The objectives of this study are as follows:

- Roughening the surfaces of Ti6Al4V implants in order to increase coating adhesion
- Depositing ZrO_2 on Ti6Al4V implant by reactive sputtering in order to inhibit Al and V ion release
- Fabrication of porous HA coating by EPD in order to enhance bone ingrowth on Ti6Al4V implants
- Self-assembly of L-Arg on HA coating in order to increase bone ingrowth and activity of bone cells on HA coating

1.3 Outline

This thesis is presented as follows: Background information of bone and joint structure, orthopedic implants and modification of Ti6Al4V orthopedic implants are reviewed in chapter 2. Experimental procedure and results are explained in chapter 3 and chapter 4, respectively. In chapter 5, the results and discussion are detailed. Finally, the conclusions of the study are presented in chapter 6.

2. BACKGROUND

2.1 Bone

Bone is an essential organ for many functions in human physiology such as support and protection of organs, movement, blood production, blood pH regulation, homeostasis, mineral storage and supplying multiple progenitor cells [20, 21]. The regulatory factors and genetic blue print facilitate bone to carry out its functions and ascertain to sustain its structure. Genetic information determines the anatomical shape of bone and is responsible for restoring that shape after fracture [22].

Bone has a complex structure which consists of a variety of materials arranged in different scales. Figure 2.1 presents the structure of bone [23, 24].

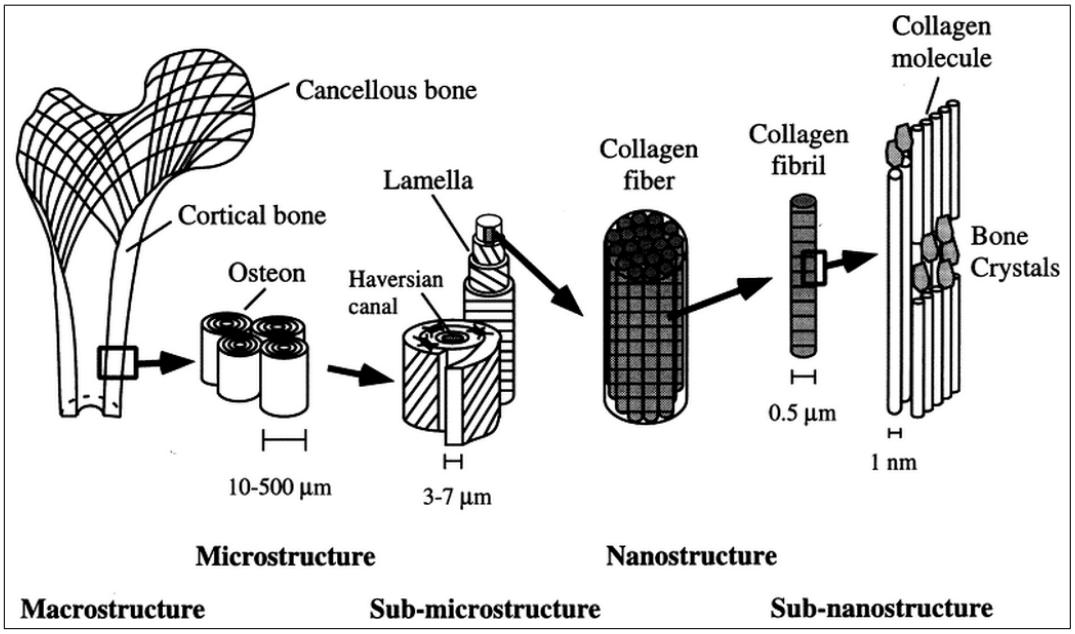

Figure 2.1 Structure of Bone [23]

Bone is distinguished into two groups which are trabecular (cancellous) and cortical (compact) at macro-level [23]. Cancellous bone is more porous than cortical bone

[25]. Moreover, cancellous bone is functionally more related to metabolic activation while cortical bone is more associated with mechanical strength [26]. At microstructure level (10-500 μm), it consists of osteons, Haversian systems and single trabeculae. At sub-microstructure level (1-10 μm), bone has a lamellae structure. Finally, bone includes its essential building blocks which are the collagen fibrils and apatite crystals at nano-level [23].

The associated cells of the bone are osteoblasts, bone lining cells, osteocytes and osteoclasts. They locate in different areas of bone. Osteoblasts, osteoclasts and bone lining cells are placed along the surface of the bone and osteocytes are found in the interior part of the bone. Osteoblasts, bone lining cells and osteocytes are originated from mesenchymal stem cells. Mesenchymal stem cells are positioned in bone marrow, periosteum, endosteum and bone canals. These cells have star-like shape and include one nucleus. They inherit small amounts of organelles and cytoplasm. They proliferate and differentiate during both endochondral and intramembranous bone formation [26]. During intramembranous ossification, mesenchymal stem cells differentiate into osteoblasts. On the other hand, they differentiate into perichondrial cells and chondrocytes during endochondral ossification. Finally, the size of perichondrial cells increase which is called hypertrophy and they differentiate into osteoblasts [25].

Osteoclasts are multi-nucleated cells which are derived from bone marrow-derived macrophages. Macrophages are originated from hematopoietic stem cells which is the other kind of stem cell found in bone [25, 26]. Hematopoietic stem cells fulfill hematopoiesis by proliferating, differentiating and self-renewal. They are the only cell type which can produce every blood cell lineages [27].

Figure 2.2 demonstrates the differentiation processes of mesenchymal stem cells and hematopoietic stem cells into osteoblasts and osteoclasts, respectively.

In Figure 2.2, there is a double-headed arrow between osteoblasts and osteoclasts, representing the balance between osteoblasts which are responsible for bone formation and osteoclasts which are responsible for bone resorption. In order to reg-

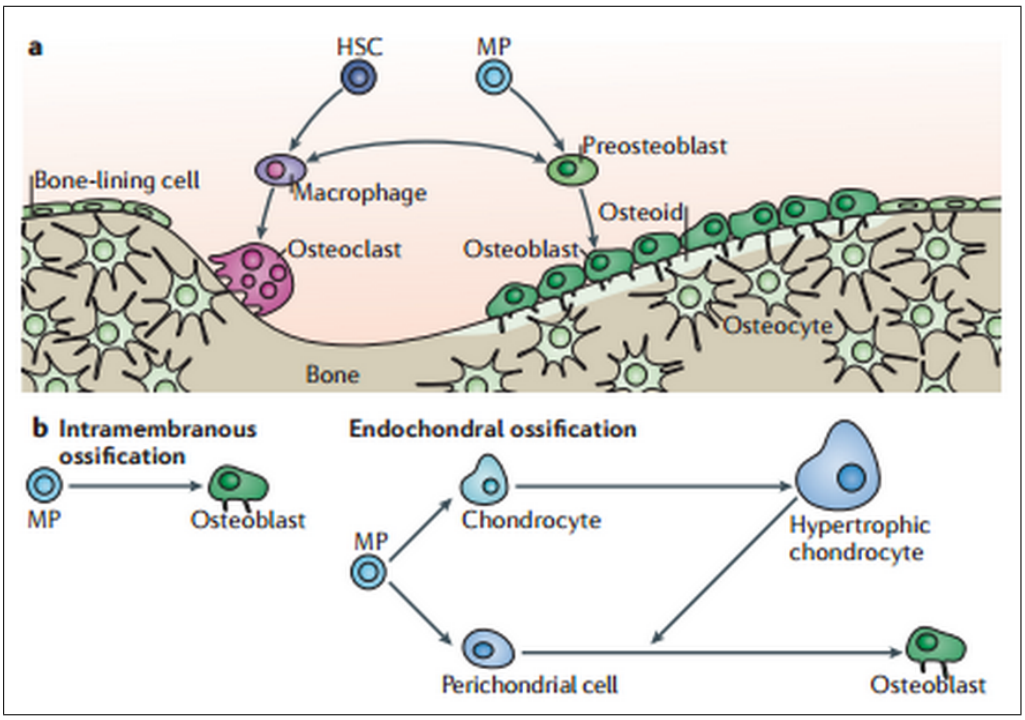

Figure 2.2 (a) Osteoblast and osteoclast cell lineages (HSC: Hematopoietic stem cell, MP: Mesenchymal stem cell), (b) The differentiation processes of mesenchymal stem cells into osteoblasts [25]

ulate the amount of bone homeostatically, osteoblasts and osteoclasts carry out their activities in balance [25, 22].

2.1.1 Bone and Joint Diseases

The common bone and joint diseases include osteoporosis, osteoarthritis, rheumatoid arthritis and infections.

Osteoporosis: Osteoporosis is a common skeletal disease in aged humans. It is often coupled with the coordinated function of osteoblasts and osteoclasts since it is characterized by low bone mass. It is also identified by degeneration of bone tissue and collapse of bone architecture, decrease of bone strength, and increase in the risk of fracture [25, 28]. The imbalance between osteoblasts and osteoclasts occurs with menopause and increasing age [28].

Figure 2.3 shows the difference between a healthy bone and an osteoporotic bone.

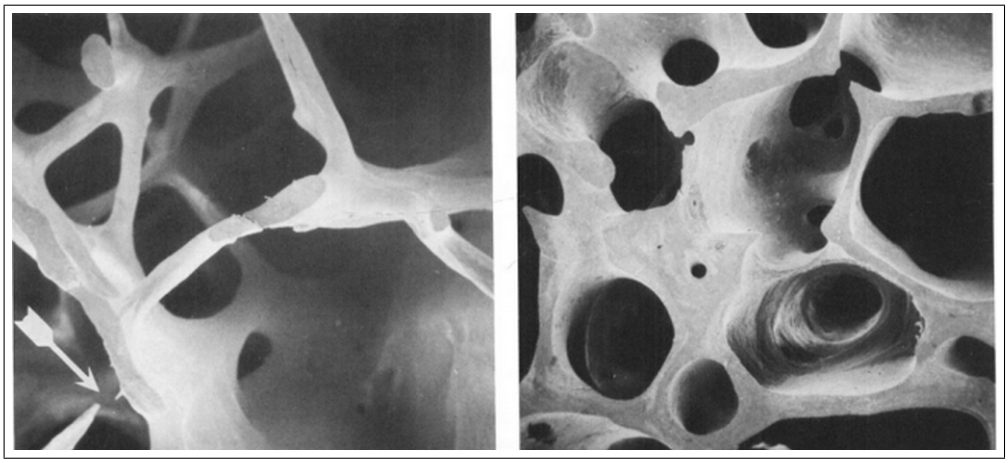

Figure 2.3 Scanning electron micrographs of osteoporotic trabecular bone (Left) and normal trabecular bone (right) [29]

As seen in Figure 2.3, healthy trabecular bone is composed of cylinders interconnected by thick bars. On the other hand, the osteoporotic bone is consisted of rods which are not connected as the arrow indicates. Therefore, the mechanical strength of osteoporotic bone is low [29].

Osteoarthritis: Osteoarthritis is a cartilage disorder related to focal articular cartilage degradation. Degradation occurs with the destruction of cartilage which triggers articular chondrocytes and synovial lining cells to produce and secrete proteolytic enzymes which degrade the cartilaginous matrix. These enzymes are aggrecanase, matrix metalloproteinase, proinflammatory cytokines and mediators such as prostaglandins and nitric oxide. This also causes a local inflammation and affects the surrounding tissue. Osteoarthritis is identified by cartilage loss, pain, joint stiffness and impairment to movement. It is a very common disease for the population involving people elder than 65 years. The people of this population have osteoarthritis in at least one of their joints [30, 31].

Figure 2.4 demonstrates an X-ray image of hip osteoarthritis.

Figure 2.4 Hip osteoarthritis [32]

Rheumatoid Arthritis: Rheumatoid arthritis is a chronic inflammatory disease. It is characterized by pain, disability, and joint destruction [33]. Rheumatoid arthritis has autoimmune component which is different from osteoarthritis [34].

Bone and Joint Infections: Bone and joint infections are generally sourced from aerobic bacteria such as Streptococcus sp., Staphylococcus sp., Enterobacteria, Enterococcus sp. and non-fermenting Gram-negative bacilli. However, bone and joint infections caused by anaerobic bacteria are rare. According to a study of Walter et al. [35], 75% of infections by anaerobic bacteria are post-operative infections. For example, most of the reported cases of anaerobic bacteria are related to post-operative shoulder infections associated with Propionibacterium acnes. Other anaerobic bacteria species, such as Clostridium sp., Bacteroidessp., Finegoldia magna, Corynebacterium diphtheroides, Parvimonas micra, Fusobacterium sp., Peptoniphilus sp., Peptostreptococcus sp. and Prevotella sp., have been reported in osteitis, septic arthritis, spondylodiscitis and orthopedic prosthesis infections.

2.2 Total Hip Arthroplasty (THA) and Total Knee Arthroplasty (TKA)

Orthopedic implants became a widespread resource for enhancing the quality of life [36]. THA and TKA are the basic surgical approaches in order to remedy osteoarthrosis and rheumatoid arthritis on knee and hip [37]-[41].

Figure 2.5 demonstrates a schematic figure of THA.

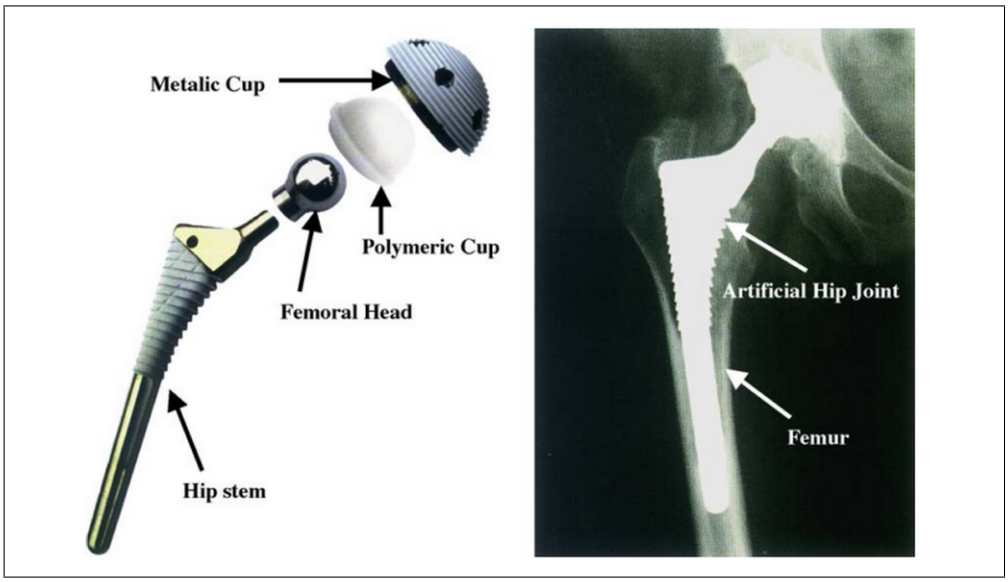

Figure 2.5 Total Hip Arthroplasty [42]

The demand for orthopedic implants is increasing as well as the number of revision surgeries. Therefore, finding new routes for expanding the lifespan of orthopedic implants and decreasing the number of revision surgeries is necessary [36, 43].

2.2.1 Failure of THA and TKA

Hip replacements may be revised due to several reasons such as aseptic loosening, infection and hip dislocation [43, 44] and the failure reasons of knee replacements may be listed as aseptic loosening, polyethylene wear, infection, instability, malalignment or malposition, deficient extensor mechanism, arthrofibrosis, avascular necrosis in the

patella, isolated patellar resurfacing and periprosthetic fracture [45]. Aseptic loosening and infection may be considered as the common failure reasons of THA and TKA which are explained below:

Aseptic loosening: The reason of aseptic loosening is osteolysis which can be related to wear debris released from the elements of prosthesis [44]. The micromotion of the prosthesis relative to bone during loading generate wear particles. These wear particles cause inflammation and bone resorption, leading to poor osseointegration [43].

Infection: Failures caused by infection have more devastating effect than aseptic loosening [46]. Patients with rheumatoid arthritis are more susceptible to infection due to anti-rheumatoid drugs and nature of the disease [47]. Early infections are generally sourced from highly virulent organisms such as or Gram-negative bacilli or S. aureus and microorganisms of low virulence, for example coagulase-negative staphylococci, are mainly the reason of late infections. Some antimicrobial agents are utilized in order to prevent infections [46]. However, a study involving 54 patients with prosthetic joint infection reveals that microorganisms can even grow on cemented prosthetics loaded with antimicrobials such as vancomysin, gentamicin and tobramycin [48]. According to Trampuz et al. [46], the result of the diagnosis depends on the stability of the implant, duration of the infection, the condition of surrounding tissue and antibiotic resistance of the pathogen. Hence, producing implants with antimicrobial properties is of great challenge.

2.3 Ti6Al4V for Orthopedic Implants

Ti6Al4V is an $\alpha+\beta$ alloy which is developed in 1950s for aerospace applications. It is extensively utilized in orthopedic applications owing to its superior mechanical strength, low density, corrosion resistance and biocompatibility [1] - [4]. These orthopedic applications are cementless orthopedic prostheses and trauma surgery implants such as screws, plates or intramedullary nails [3]. However, Ti6Al4V has some drawbacks which restricts its usage as an implant.

Ti6Al4V shows low hardness and wear resistance in aggressive environment [49, 50]. Moreover, Al and V ions may release to the surrounding tissue. Al and V can cause long-term health problems [51, 52]. Furthermore, osseointegration of Ti6Al4V is inadequate [6, 50]. Therefore, some modification techniques have been developed in order to amend the surface of Ti6Al4V implants. These are listed as follows [42, 53, 54]:

- Machining, polishing, grinding, blasting
- Chemical etching
- Modification with bioceramic layers
- Modification with bioglass and bioactive glass ceramic layers
- Modification with biomolecules

2.4 Bioceramic Coatings

2.4.1 Bioinert Ceramic Coatings

Nitrides, carbides, Al_2O_3 and ZrO_2 are classified in bioinert ceramics. Bioinert ceramic coatings have mostly been studied in order to enhance the hardness, wear and corrosion resistance of Ti6Al4V implants [42].

2.4.1.1 ZrO_2. ZrO_2 is a non-resorbable bioinert ceramic which has superior strength and toughness than other ceramic materials. Superior mechanical properties and longevity of ZrO_2 make it preferred in implant industry [55]. Today, it is utilized as femoral head in THA [56].

ZrO_2 exhibits in three different crystalline structures which are monoclinic, tetragonal and cubic. ZrO_2 is in monoclinic form at ambient temperature. With increasing temperature to $\approx 1170°C$ and $\approx 2370°C$, it transforms into tetragonal and

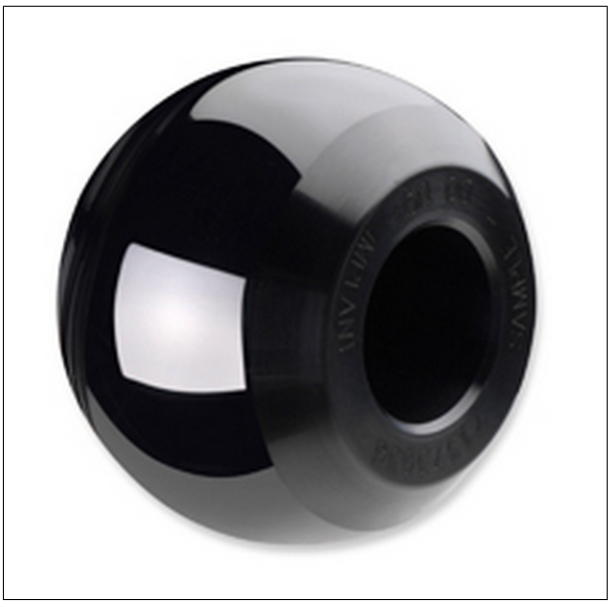

Figure 2.6 Zr-Nb (2.5% Nb) Femoral Head with a Thermally Oxidized Surface- Brand Name: Oxinium

cubic phases respectively. Cooling tetragonal ZrO_2 make it transform back into monoclinic phase in a destructive martensitic mechanism which is diffusionless and displacive. Moreover, this transformation causes a 4 % volume expansion. It is possible to produce metastable tetragonal and cubic phases at ambient temperature by adding aliovalent cations into its crystal structure. Incorporation of some oxides such as Y_2O_3, CaO, CeO_2 and MgO provides more symmetric tetragonal and cubic structures [57].

Y_2O_3 stabilized ZrO_2 is considered as the most appropriate for medical implants [57, 58]. $(Y_2O_3)_x(ZrO_2)_{1-x}$ consists of $0.02<x<0.09$ and $0.04<x<0.4$ retains tetragonal and cubic phases at ambient conditions, respectively. This means a Y/(Y+Zr) molar ratio of 4–17 % and 8–57 % [57]. In addition to dopants, grain size has a decisive effect on the metastability of tetragonal phase. According to Garvie' s theory, small crystallite size decreases the transformation temperature. Crystallite size effect is explained by the difference of the surface energies of monoclinic and tetragonal phases, balancing for the chemical free energy. 30 nm is the critical diameter to obtain metastable tetragonal ZrO_2 [59, 60].

Despite the progress of the techniques to keep tetragonal ZrO_2 in a metastable state, the retrieval studies demonstrated the increase of monoclinic phase on tetragonal ZrO_2 femoral heads [61]. Tetragonal zirconia destabilizes in water or water vapor [62]. This is called low temperature degradation. The filling of oxygen vacancies in tetragonal ZrO_2 structure with water species is considered as the main cause for destabilization [63]. The other reasons of transformation may be heat and pressure [64]. Low temperature degradation accelerates by micro-cracks, pores and increased roughness [62]. The retrieved heads showed increased roughness, wear and decreased hardness [63, 64]. The increase in wear rate of femoral heads is related to surface transformation which is associated with sphericity and increased roughness. Wear particles can induce macrophage reaction by entering the periprosthetic tissues. Macrophages starts osteoclastic bone resorption by releasing pro-inflammatory cytokines, leading to osteolysis and replacement of the implant [63].

The Deposition Techniques of ZrO_2: The deposition techniques of ZrO_2 include physical vapor deposition (PVD) [65, 66], plasma spraying, magnetron sputtering [66] and electrochemical methods such as anodization [67], microarc oxidation [68] and EPD [69].

Magnetron sputtering has become a preferred technique for a variety of industrial coatings. Magnetron sputtering is a promising technique in order to produce corrosion resistant, hard and wear-resistant coatings [70]. In basic magnetron sputtering process, inert gas is ionized by an external power supply and produces plasma. Glow discharge plasma bombards target material by energetic ions and removes atoms from target material. These atoms condense on substrate material to produce a thin film [70, 71].

Figure 2.7 schematizes the process of sputtering.

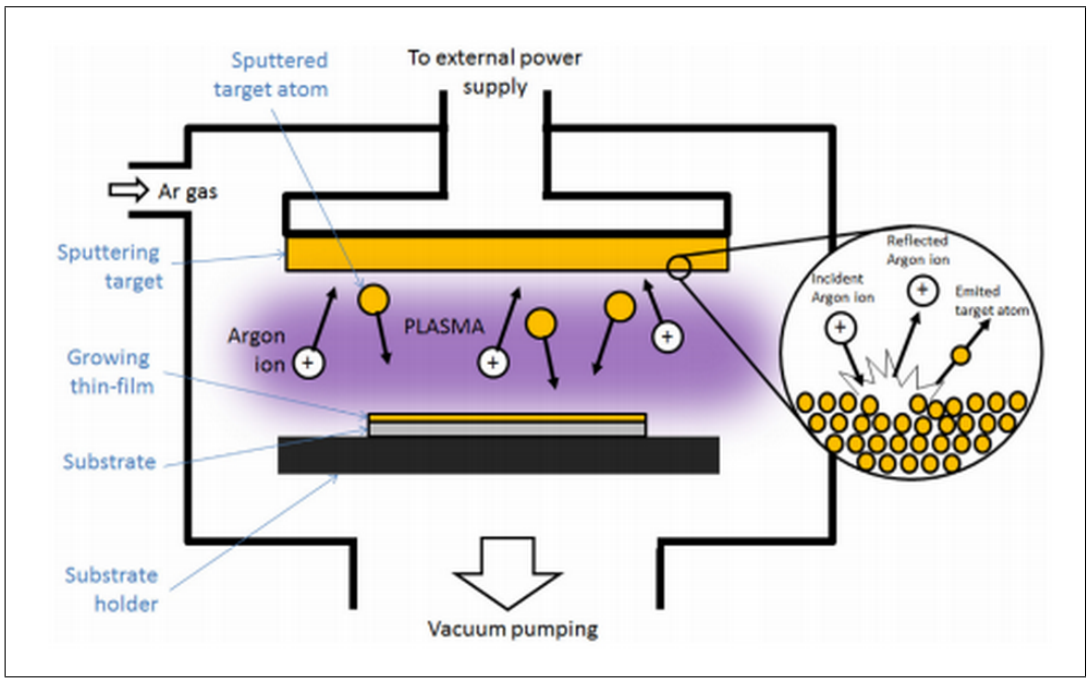

Figure 2.7 Sputtering Process [71]

In some applications, a reactive gas takes part in the process with an inert gas. This technique is called reactive gas sputtering. The reactive gas can be O_2 or N_2. In this technique, the dissociation products of reactive gas react with the target while the inert gas ions bombard the target [71].

2.4.2 Bioactive Ceramic Coatings

TiO_2, bioactive glass ceramics and calcium phosphates are bioactive ceramics [72, 73]. Bioactive ceramics provide direct bonding with living tissues [72].

2.4.2.1 Hydroxyapatite. Calcium phosphates have similar composition and structure to the apatite in human bones. The example of calcium phosphates are β-tricalcium phosphate (β-$Ca_3(PO_4)_2$), hydroxyapatite (HA, $Ca_10(PO_4)_6(OH)_2$) and biphasic calcium phosphate which consists of both β-tricalcium phosphate [9, 74].

HA is the thermodynamically most stable phase among calcium phosphates under physiological conditions [75]. The crystalline structure of HA is shown in Figure 2.8.

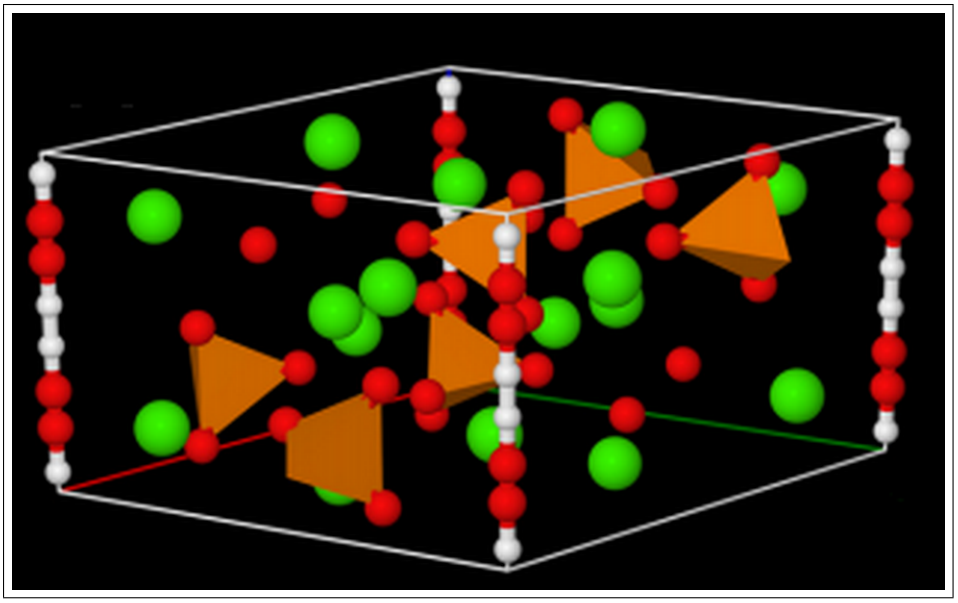

Figure 2.8 The Crystalline Structure of HA (Green, red, orange and white symbols represent Ca, O, P and H respectively)[76]

HA is extensively studied in biomedical research and industry due to its strong bioactivity and osteoconductivity which promotes bone formation and biological fixation [74, 77, 78]. Moreover, it is non-inflammatory, non-toxic and causes no immunological or fibrous reaction [79]. However, HA coatings can suffer from high tensile stress on Ti6Al4V implants due to the mismatch of the coefficient of thermal expansion between Ti6Al4V and HA. This causes low adhesion strength of HA coatings [80].

The Deposition Techniques of HA: The deposition techniques of HA include plasma spraying [77, 81], magnetron sputtering [66, 82], dip coating [78, 83], sol-gel [84, 85] and EPD [86, 87].

EPD is an effective method to produce ceramic coatings on metallic substrates. However, the research field of EPD is not limited to ceramics. It is also extensively utilized to deposit bioactive glass, carbon nanotubes, drugs and biological molecules such as proteins, enzymes, polysaccharides and cells. This technique has so many

advantages including low cost and simplicity. It is a versatile technique to be used for material combinations with different patterns. It is also an effective technique to produce porous bioactive coatings as well as to coat porous and textile substrates [88]. Moreover, it can be operated at ambient temperature [88, 89].

EPD is based on a two-step process. First step is electrophoresis and the second one is deposition [90]:

Electrophoresis: Electrophoresis is the migration of the charged molecules which are dispersed in a suspension toward the deposition electrode in an electric field. The molecules in the suspension can acquire surface charge in different mechanisms such as by dissociating ions into solvent, adsorbing ions from solvent or electron transfer with the solvent.

Deposition: Deposition is the accumulation of the molecules on the surface of the oppositely charged electrode, a substrate which is connected to an electrode or placed in between the electrodes.

Figure 2.9 is a schematic presentation of EPD.

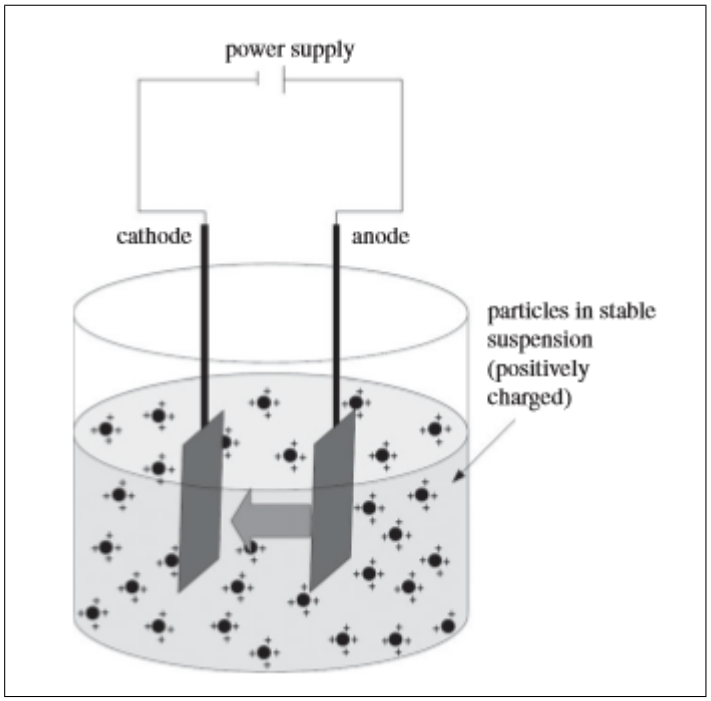

Figure 2.9 EPD Process [88]

2.5 Arg in Biomedical Studies

Biomolecules including proteins or specific amino acids have gained interest in biomedical studies since they are important molecules for living organisms [91]. Compared to proteins or peptides, amino acids are preferred for clinical applications since they are more stable molecules and less expensive [16].

Figure 2.10 presents the molecular structure of arg.

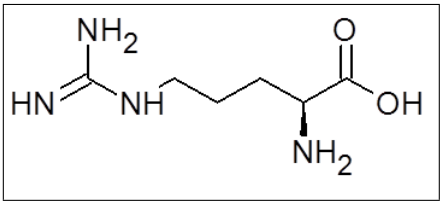

Figure 2.10 Molecular Structure of L-Arg (drawn on ChemSketch)

Arg is a cationic amino acid in physiological conditions [17]. Many studies have demonstrated the antimicrobial properties of cationic amino acids such as lysine and arg. These amino acids make bidentate hydrogen bonding and cation-π interactions with the lipopolysaccharide, teichoic acid and phosphatidyl glycerol phospholipid head groups on the surface of the bacterial cellular walls and disrupt its structure by forming a pore within the bacterial wall or change its permeability. This leads them to enter the interior of the bacterial cell and affect its cellular functions [92, 93].

According to the study of Shafer et al. [94], the structure of guanidinium is the primary agent for antimicrobial activity. The activity of an arg–rich peptide against methicillin-resistant S. aureus decreased when four arg residues were replaced with lysine residues. This shows that cationic charge is not enough for potent antimicrobial activity and arg interacts specifically with bacteria surface. Stronger interaction and higher activity is associated with the higher potential of guanidinium group to make hydrogen bonding in the formation of salt bridges [92, 94].

In addition to antimicrobial studies, the potential benefits of cationic charge of arg has been practiced in many studies in order to enhance protein binding of HA [18]. HA interacts with bovine serum albumin by the bond between Ca^{2+} and -COO^{-}. According to Lee et al. [18] , arg provides -NH^{3+} groups and increases the number of cations on HA to interact with -COO- on bovine serum albumin. Lee et al. also indicates the lower affinity of arg to positively charged proteins. The high bioactivity of Arg/HA coating was demonstrated by Gonzalez-McQuire et al. [11]. An even calcium phosphate layer was formed on Arg/HA coated titanium after immersion in T-SBF for 5 days. They also presented self-repair property of Arg/HA coating after scratch test.

The studies with mesenchymal stem cells showed the positive effect of arg on proliferation at early stage. Moreover, arg increased mRNA expression of osteogenic gene expression markers which are alkaline phosphatase, type Iα1 collagen and osteocalcin. Further investigations also demonstrated the increase of mRNA expression of the transcription factors which are osterix, Runx2 and DIx5 which are key agents for stimulating osteoblast-specific gene expression with the addition of arg. According to

Huh et al. [19], arg increases osteoblastogenesis by controlling Wnt/β-catenin independent signaling and the mechanisms including NFATc that regulate MSC fate and differentiation. The study of Vater et al. [12] also revealed that arg increased the adhesion, proliferation and ALP activity of bone marrow derived mesenchymal stem cells on calcium phosphate cements. Overall, arg is a promising material for biomedical applications and has great potential to enhance osseointegration of HA coatings.

3. MATERIALS AND METHODS

3.1 Surface Treatment of Ti6Al4V Substrates

As-obtained Ti6Al4V substrates were firstly polished by a micropolisher (Proxxon D-54518). The substrates were then ultrasonically cleaned in acetone, isopropanol and distilled water for 15 minutes, respectively. The clean samples were dried with N_2. Subsequently, these samples were etched in HCl:distilled water:H_2SO_4 solution (1:2:3, v/v/v) in water bath (Isolab) at 60 °C for 4 hours and rinsed with water. Figure 3.1 shows the color change of colorless acid solution to violet after acid etching process.

Figure 3.1 Etchant solution after 4-hour-treatment

Violet color occurs due to the formation of Ti^{3+} salts by the oxidation of titanium in acid solution [95].

3.2 Characterization of Etched Substrates

3.2.1 Scanning Electron Microscopy (SEM)

Surface morphology of pristine and etched Ti6Al4V substrates were examined by SEM (Philips XL30 ESEMFEG/EDAX) in secondary electron mode without any sputter coating at Boğazici University Research and Development Center. The applied voltage was 10 kV and the surfaces were magnified by 100x, 500x, 2000x, 5000x, 10000x, 20000x and 50000x.

3.2.2 Stylus Profilometer

Roughness measurements were carried out by using Dektak Profilometer (Bruker Dektak XT) at clean room of Center for Life Sciences and Technologies. The average R_a, R_z and R_q values were measured on three samples by evaluating five different lines with a length of 55000 μ for 400 seconds. The applied cut-off length was 0.8 mm.

3.3 Deposition of ZrO_2 by Reactive DC Magnetron Sputtering

Reactive sputtering process was conducted in the system designed and manufactured by Vaksis R&D and Engineering. The etched substrates were placed in deposition chamber and base pressure of below $5x10^{-7}$ Torr was achieved. Then, the temperature of the substrates was increased to 200 °C and 50 sccm Argon gas was pumped into the system. Subsequently, the volume of Argon was decreased to 30 sccm and 20 sccm O_2 gas was pumped into the chamber. Before the process was initiated, the sputtering power was increased to 200 W in the rate of 40 W/min and the target was pre-sputtered for 5 minutes in order to clean the surface of the Zr target and stabilize the process. Finally, the substrate stage rotated at 15 rpm and reactive sputtering was performed for 4 hours. The parameters of sputtering process are given at Table 3.1.

Table 3.1
Reactive sputtering parameters

Base Pressure (Torr)	Below $5x10^{-7}$
Substrate to Target Distance (cm)	13
Substrate Temperature (°C)	200
Flow Rate of Ar (sccm)	30
Flow Rate of O_2 (sccm)	20
Sputtering Pressure (Torr)	$5x10^{-3}$
Sputtering Power (W)	200
Bias Voltage (V)	295-302
Sustrate Rotation Rate (rpm)	15
Sputtering Duration (h)	4

Figure 3.2 demonstrates the ZrO_2-coated Ti6Al4V samples.

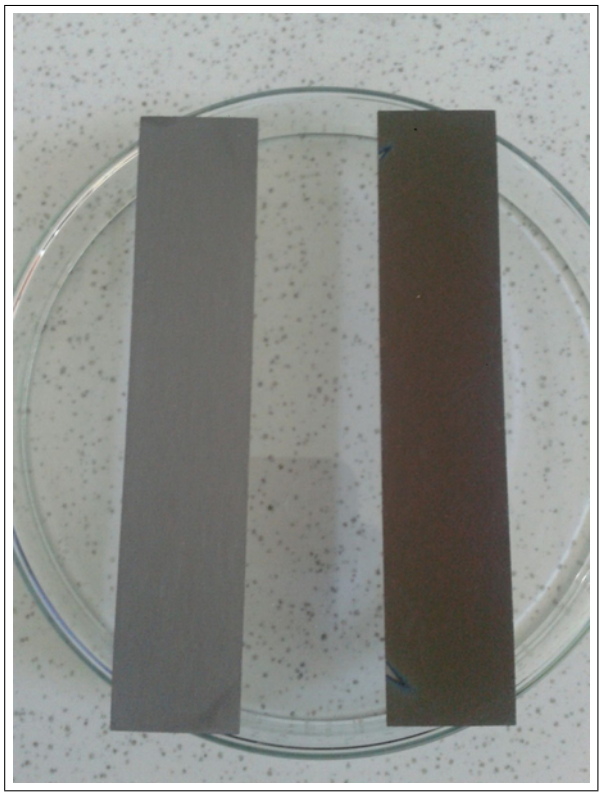

Figure 3.2 Ti6Al4V samples not coated (left) ZrO_2-coated (right)

3.4 Characterization of ZrO_2 Coatings

3.4.1 SEM

Morphology of reactively sputtered ZrO_2 coatings were evaluated by SEM (Philips XL30 ESEMFEG/EDAX) in secondary electron imaging mode by applying a voltage of 10.0 kV at Boğazici University Research and Development Center. The samples were not coated by sputtering. The surfaces were magnified by 100x, 500x, 2000x, 5000x, 10000x, 20000x and 50000x.

3.4.2 Raman Spectroscopy

The type of crystalline structure of ZrO_2 coating was determined by using Raman Spectroscopy (Renishaw-INVI Reflex Confocal Raman System) with an excitation wavelength of 532 nm from a green light laser at Ahmet Keleşoğlu Faculty of Education in Necmettin Erbakan University.

3.4.3 XRD

XRD spectrum of ZrO_2 coating was obtained by using Bruker D8 Advance with Cu Kα radiation (λ=1.540 $\tilde{A}$) at Surface Science and Technology Center in Koç University. The data were collected between 0°-90°. The slit size was 1 mm.

3.5 Production of HA Coatings by EPD

3.5.1 Preparation of HA Suspension

A previously reported method was modified to prepare HA suspensions [96]. 1 g HA was dissolved in 35 ml isopropanol and magnetically stirred for 1 hour. The

applicable suspension with dispersion stability was obtained by ultrasonic agitation and magnetic stirring of HA nanoparticles for 3 hours. The pH of the final suspension was 6.

3.5.2 EPD

ZrO_2-coated Ti6Al4V was utilized as anode and stainless steel was used as electrode. The distance between anode and cathode was 2 cm. The applied voltage was 30 V and the duration of the deposition process was 205 s at room temperature. Figure 3.2 shows the experimental setup of EPD.

Figure 3.3 Experimental setup for EPD

Finally, the HA coatings were dried at room temperature for 24 hours.

3.5.3 Sintering of HA Coatings

HA coatings were sintered at 600 °C for 1 hour in ambient atmosphere [97] in the furnace (Thermo Fisher- K114).

3.6 Functionalization of HA Layer with L-Arg

0, 174 g L-Arg was dissolved in 50 ml phosphate buffered saline (pH=7.4). HA-coated samples were immersed in the prepared solution and incubated at room temperature for 24 hours. The half of the HA-coated samples were coated with L-Arg and the others were kept as control.

3.7 Characterization of HA and L-Arg/HA Coatings

3.7.1 SEM

Surface morphology of HA and L-Arg/HA coatings was examined by using SEM (Philips XL30 ESEMFEG/EDAX) at Boğazici University Research and Development Center. The samples were coated with platinum by using Polaron SC7640 for 60 seconds before SEM analysis. The applied voltage and plasma current were 1.8 kV and 25-27 mA, respectively. SEM micrographs were taken by applying voltage of 10 kV in secondary electron mode.

3.7.2 FTIR

The compositional changes of HA coatings after incubation in L-Arg solution and the binding mechanism of HA and L-Arg was figured out by using FTIR (Thermo Scientific Nicolet). 32 scans were collected in the range from 4000 cm^{-1} to 500 cm^{-1} at resolution of 2 cm^{-1}.

3.7.3 XPS

XPS measurements of HA and L-Arg/HA coatings were performed by using Thermo Scientific K-Alpha X-ray Photoelectron Spectrometer. This instrument was equipped with Al Kα micro-focused monochromator. Spot size was 400 μ.

3.7.4 Ninhydrin Test

Ninhydrin is used to detect the free amine groups on the surface [98, 99]. A previously reported method by Kim et al. [99] was used. HA-coated and L-Arg/HA coated samples were immersed in ninhydrin solution which had a concentration of 1 mol/l in ethanol for 1 minute. Subsequently, the samples were taken into glass petri dishes and covered. Then, they were incubated at 37 °C for 15 minutes. The color changes were photographed.

4. RESULTS

4.1 Surface Treatment of Ti6Al4V Substrates

SEM images of unetched and etched Ti6Al4V are shown in Figure 4.1.

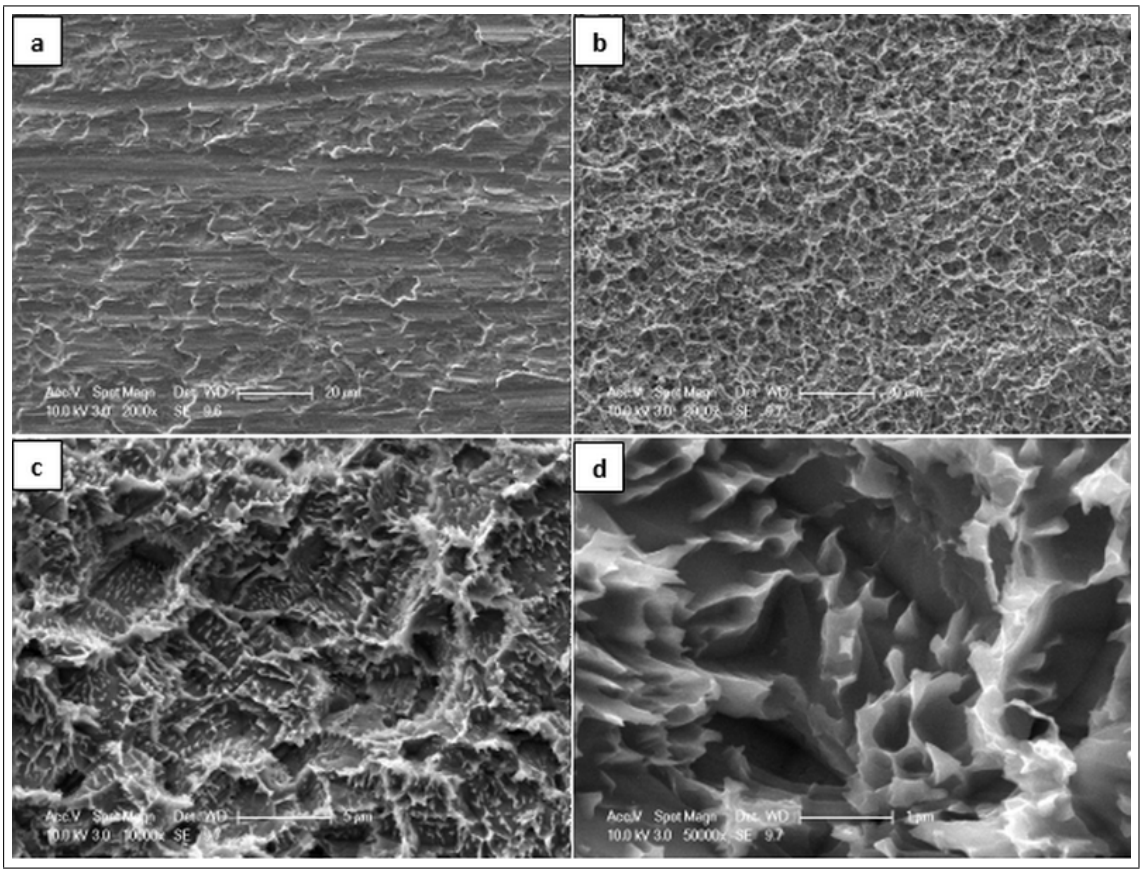

Figure 4.1 (a) Pristine (2000x, scale bar: 20 μm) and etched Ti6Al4V substrates in different magnifications (b) 2000x, scale bar: 20 μm (c) 10000x, scale bar: 20 μm (d) 50000x, scale bar: 1 μm

According to Figure 4.1, unetched Ti6Al4V has a smooth surface with a few parallel grooves and etching of Ti6Al4V in HCl:distilled water:H_2SO_4 solution for 4 hours changes its morphology significantly. Etching process formed a rougher surface with many nano pits. The roughness results are given in Table 4.1.

Table 4.1
The R_a, R_q and R_z values of etched Ti6Al4V substrates

Line 1 (μ)	Line 2 (μ)	Line 3 (μ)	Line 4 (μ)	Line 5 (μ)	Average (μ)
R_a: 4.35	R_a: 4.04	R_a: 4.43	R_a: 4.34	R_a: 4.31	R_a: 4.29
R_q: 5.27	R_q: 4.87	R_q: 5.37	R_q: 5.20	R_q: 5.21	R_q: 5.18
R_z: 21.50	R_z: 20.99	R_z: 22.11	R_z: 22.07	R_z: 21.30	R_z: 21.59
R_a: 3.76	R_a: 4.11	R_a: 3.70	R_a: 4.54	R_a: 3.92	R_a: 4.01
R_q: 4.67	R_q: 5.00	R_q: 4.56	R_q: 5.54	R_q: 4.82	R_q: 4.92
R_z: 20.35	R_z: 20.99	R_z: 19.67	R_z: 23.25	R_z: 20.52	R_z: 20.96
R_a: 4.14	R_a: 4.31	R_a: 4.30	R_a: 4.34	R_a: 4.39	R_a: 4.30
R_q: 5.06	R_q: 5.32	R_q: 5.25	R_q: 5.27	R_q: 5.41	R_q: 5.26
R_z: 22.24	R_z: 21.73	R_z: 21.45	R_z: 21.99	R_z: 22.53	R_z: 21.99

The R_a value of substrates increased from 0.4 μ to 4.20 μ by etching process.

4.2 ZrO_2 Coating

Figure 4.2 presents the SEM micrographs of ZrO_2 coating.

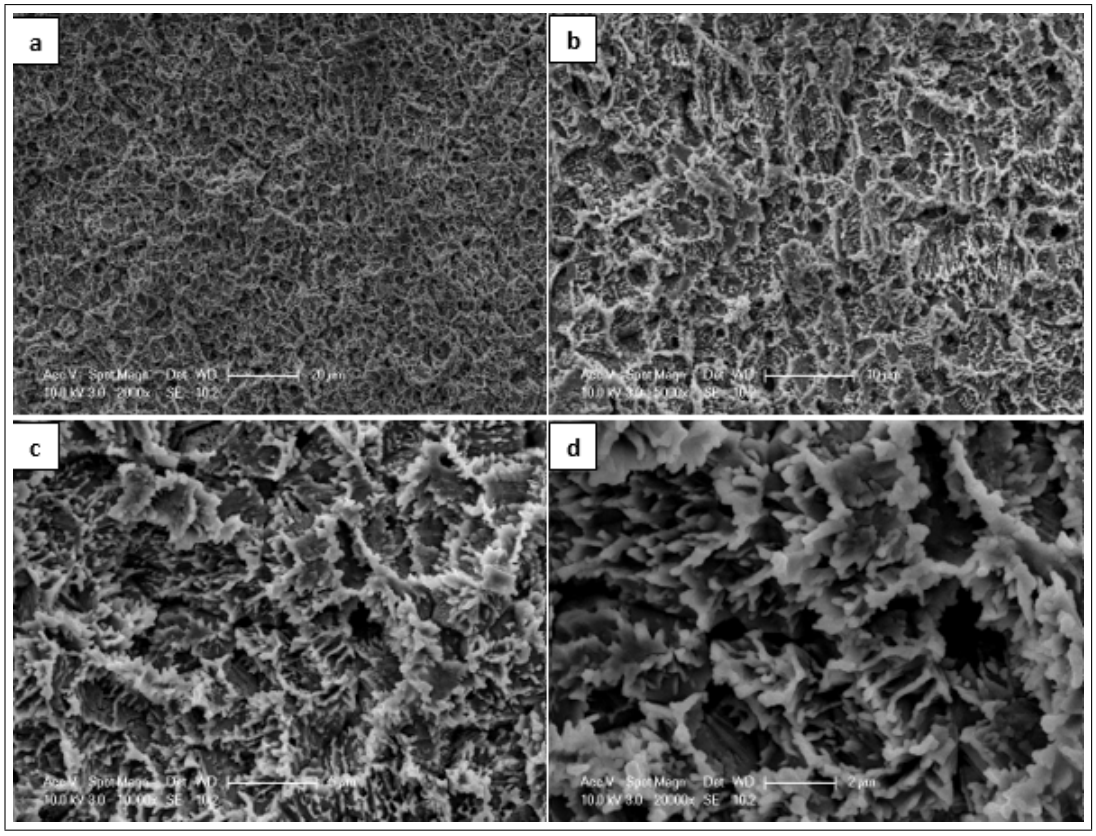

Figure 4.2 SEM images of ZrO_2 coating on etched substrates in magnifications of (a) 2000x, scale bar: 20 μm (b) 5000x, scale bar: 10 μm (c)10000x, scale bar: 5 μm (d) 20000x, scale bar: 2 μm

Figure 4.2 demonstrates that Ti6Al4V kept its rough morphology since ZrO_2 film was thin. Raman and XRD spectrums of ZrO_2 coating reveal the crystalline structure of ZrO_2 coating. These spectra are shown in 4.3 and 4.4, respectively.

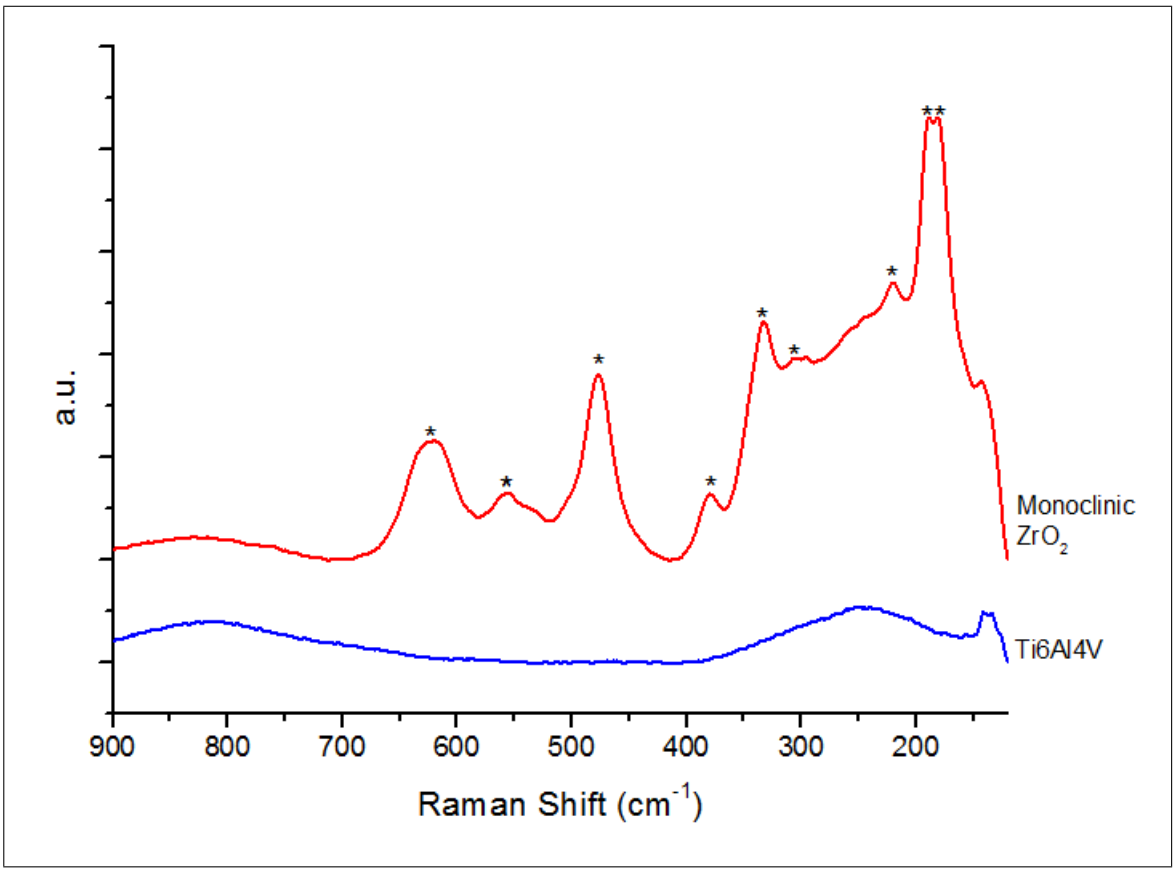

Figure 4.3 Raman spectrum of ZrO_2 coating

The doublet at 181 and 189 cm^{-1} and the broad peak at 477 cm^{-1} are the most distinct characteristic bands of monoclinic ZrO_2. The other characteristic peaks of monoclinic ZrO_2 which are at 306, 333, 380, 555 and 621 cm^{-1} can also be identified on Raman spectrum [100, 101].

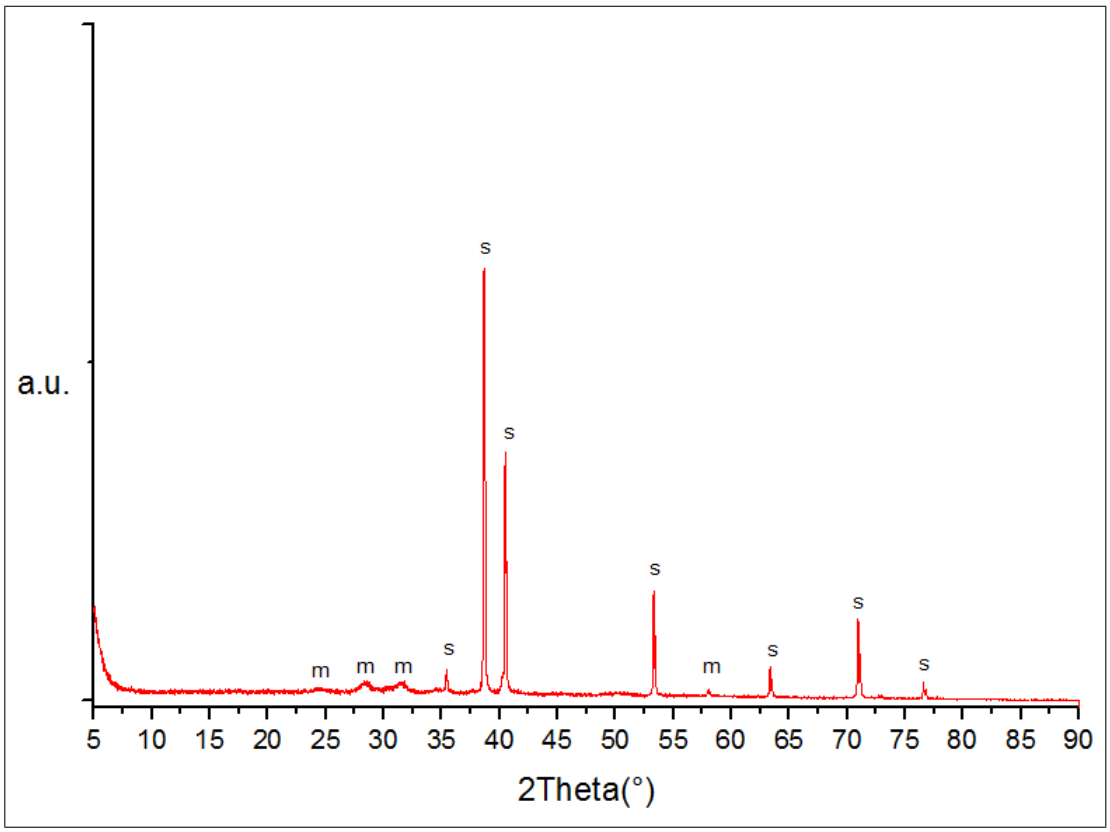

Figure 4.4 XRD spectrum of ZrO_2 coating (m: monoclinic, s: substrate)

On XRD spectrum, the peaks correspond to monoclinic ZrO_2 and substrate. No peaks related to tetragonal structure are observed in the XRD spectrum. Moreover, Appendix A shows the software scan which approves that the coating has single phase. The most intense peaks of monoclinic ZrO_2 can be identified at 28.2° and 31.5°. These peaks are related to (1 Ì11) and (111) structures, respectively.

4.3 HA Coating

Figure 4.5 shows the SEM image of HA coatings.

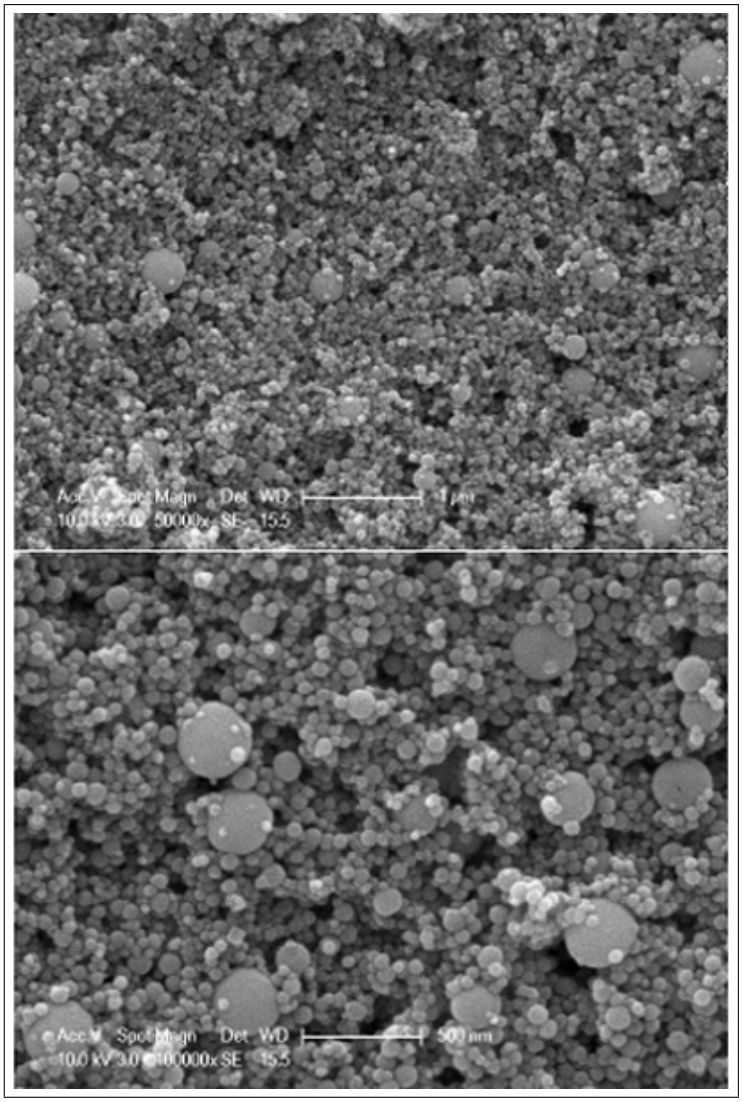

Figure 4.5 SEM micrographs of HA coating in different magnifications (a) 50000x, scale bar: 1 μm (b) 100000x, scale bar: 500 nm

As can be seen in Figure 4.5, HA coating has a porous structure which facilitates bone-implant interaction. Since there was no agglomeration, the difference of the particle sizes might be due to the size variation of the commercial HA particles which was below 200 nm. Similar SEM images were obtained by Drevet et al. [87] who utilized the same commercial HA particles in their studies.

Figure 4.6 shows the XRD spectrum of HA coating.

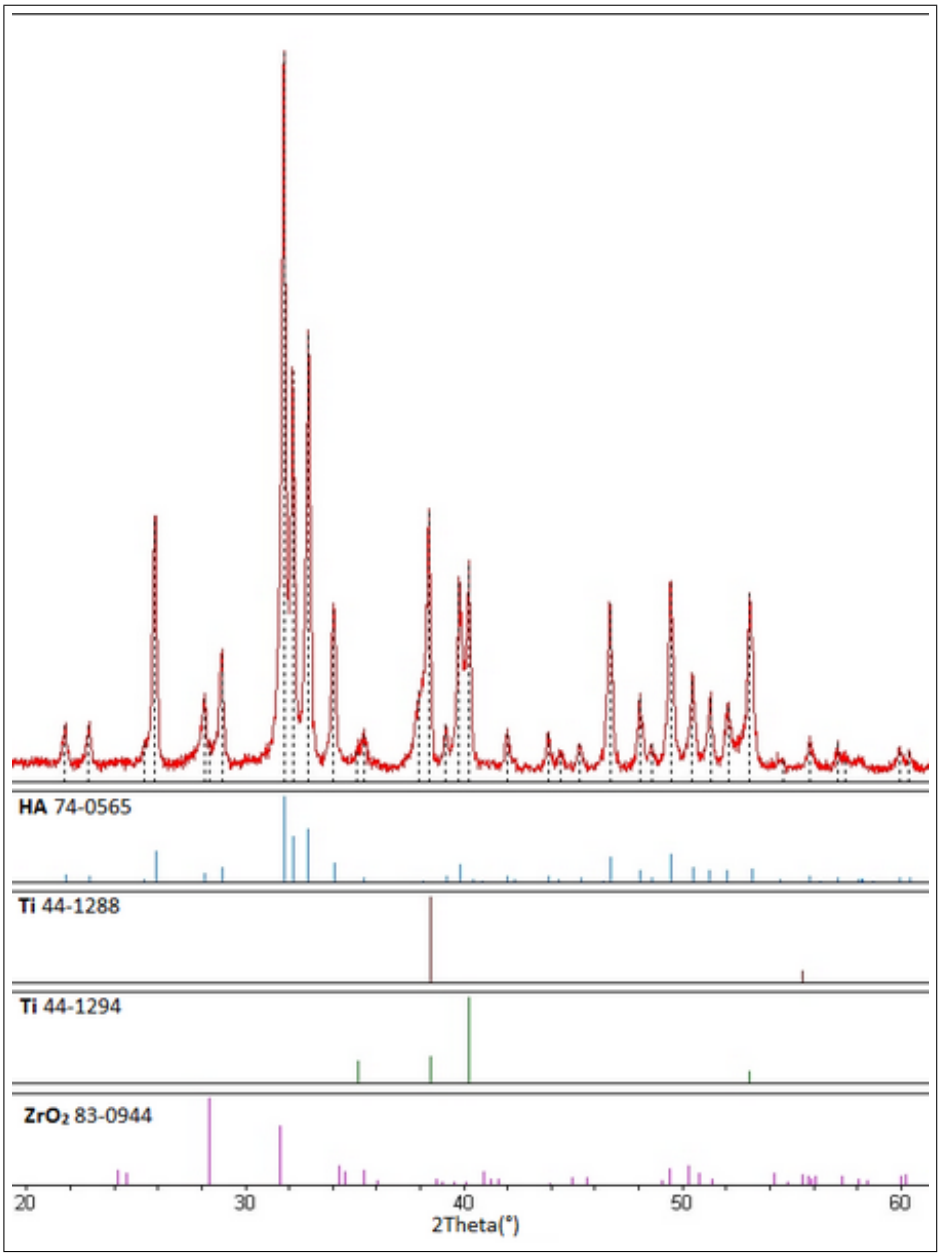

Figure 4.6 XRD spectrum of HA coating

XRD spectrum of HA coating reveals that HA is the only calcium phosphate structure in the coating after sintering and there are no impurities.

4.4 Functionalization of HA coating with L-Arg

Figure 4.7 presents SEM images of L-Arg/HA coating.

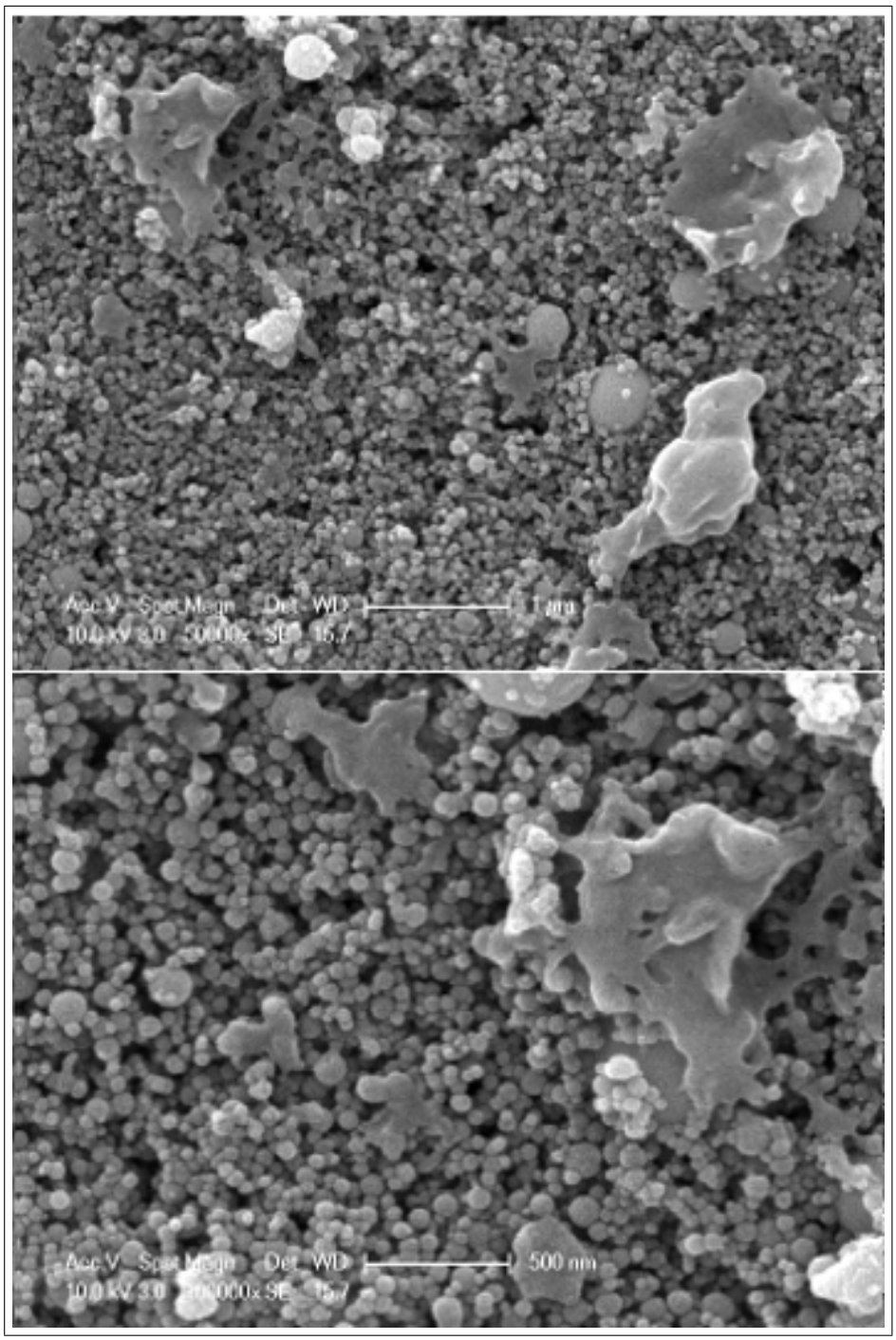

Figure 4.7 SEM micrographs of L-Arg /HA coating in different magnifications (a) 50000x, scale bar: 1 μm (b) 100000x, scale bar: 500 nm

SEM images of L-Arg/HA coating shows the irregular aggregates of self-assembled L-Arg nanoparticles as can be observed in many previous studies [102] - [104]. FTIR spectrums are presented in figure 4.8.

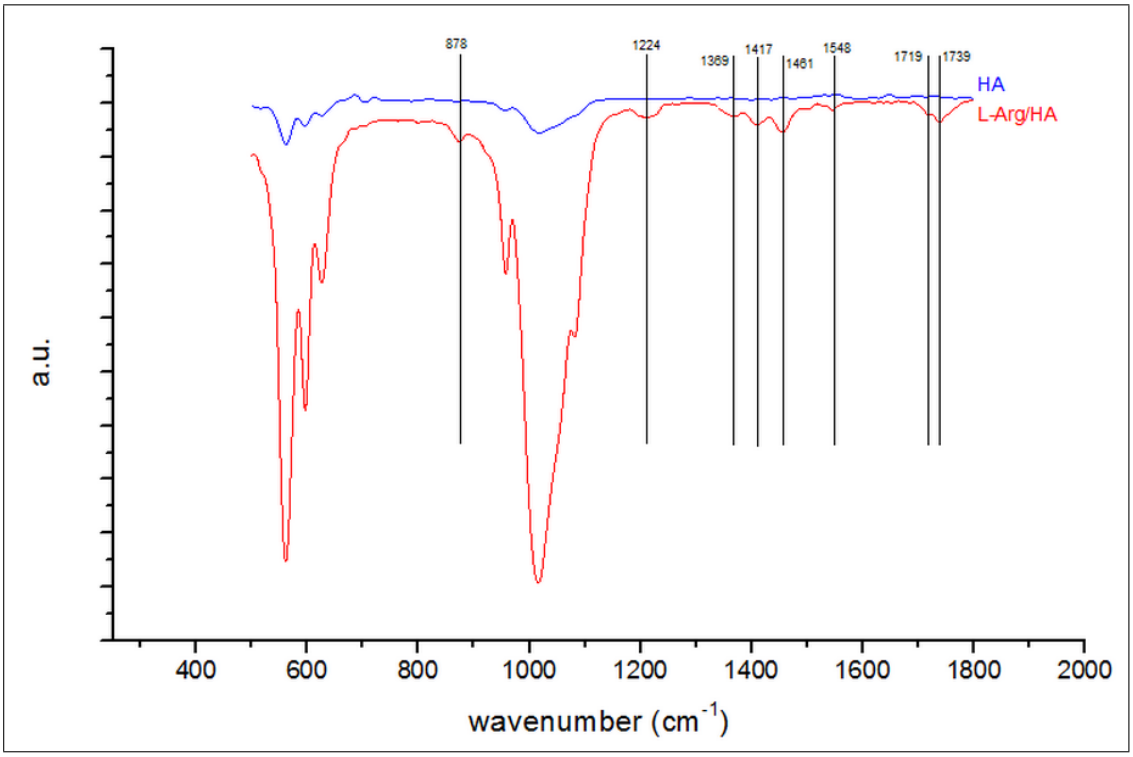

Figure 4.8 FTIR spectrums of HA and L-Arg/HA coatings

On the FTIR spectrum of HA coating, the peaks at 561, 591, 956, 1018, 1083 cm^{-1} refer to -PO_4^{3-} group and the peak at 628 cm^{-1} refers to -OH group. Many different peaks can be observed on the spectrum of L-Arg/HA coating, including 878, 1224, 1369, 1417, 1461, 1548, 1719 and 1739. The peaks at 878, 1417 and 1461 cm^{-1} correspond to the CO_3^{2-} which is sourced from atmospheric CO_2 dissolved in L-Arg solution. The peak at 1224 cm^{-1} refers to C-N bond [16]. The peaks at 1369 and 1548 cm^{-1} refer to the asymmetric C-O stretch in carboxyl group [75, 105]. The peak at 1739 cm^{-1} accompanied with the peak at 1719 cm^{-1} is an evidence of the protonated carboxyl group. These peaks can be attributed to carbonyl stretching of carboxyl group [106].

C1s spectrums of HA and L-Arg/HA coatings are shown in Figure 4.9.

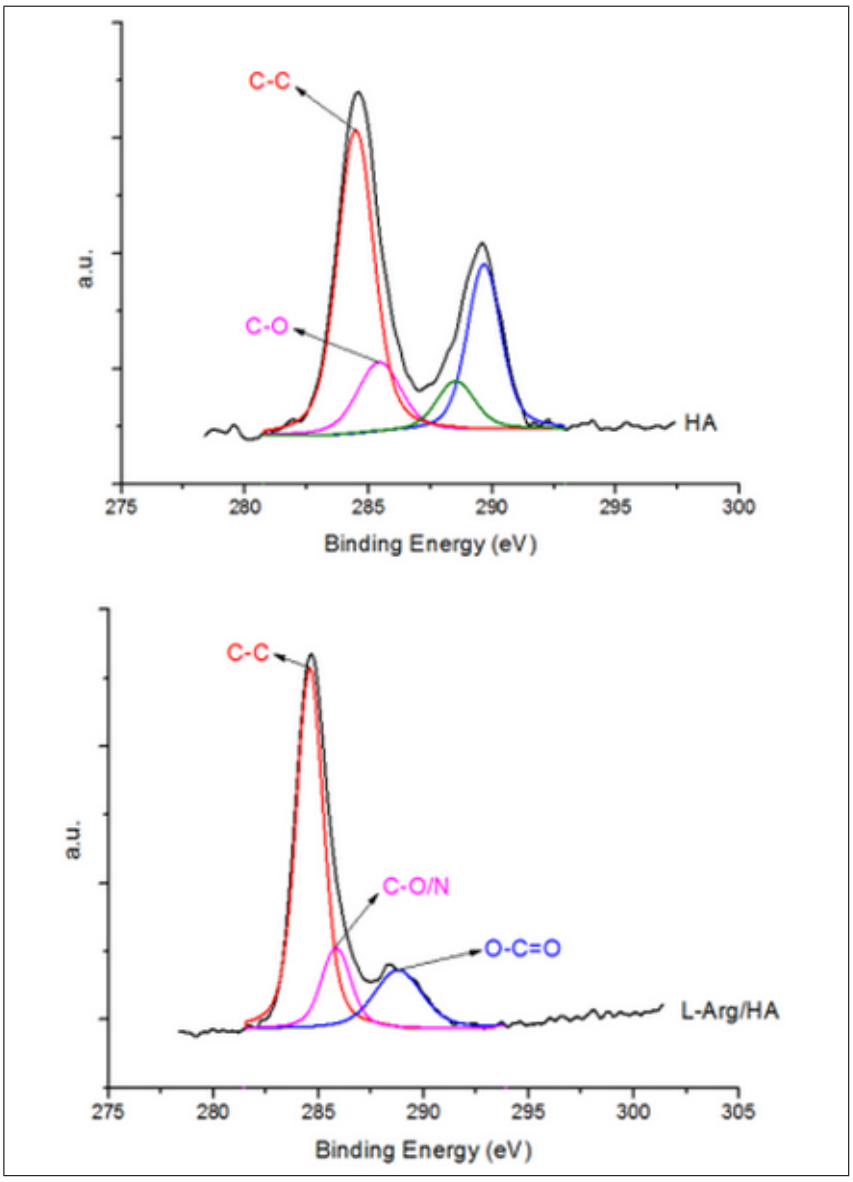

Figure 4.9 C1s spectrums of HA and L-Arg/HA coatings

C1s spectrum of HA reveals the carbon contamination of HA coating which was recorded for many studies [107] - [109]. The peaks at 284.37 eV and 285.33 eV refer to the C-C and C-O bonds due to the carbon contamination, respectively [109]. The other peaks at 288.41 eV and 289.56 eV are recorded as the other oxidized forms of carbon in previous studies [108, 109]. C1s spectrum of L-Arg/HA coating demonstrates the arise of new peaks at 285.74 eV and 288.69 eV. These peaks correspond to C-O/N and O-C=O bonds which are related to the functional groups of L-Arg [110].

Table 4.2 presents the changes in the atomic percentages with the incorporation of L-Arg to HA.

Table 4.2
Ca/P and C/Ca ratios of HA and L-Arg/HA coatings

	HA-coated	L-Arg/HA-coated
Ca/P	1.50	1.39
C/Ca	0.42	0.79

According to Table 4.2, Ca/P ratio decreased and C/Ca ratio was increased with the incorporation of L-Arg to HA coating.

Figure 4.10 presents the results of ninhydrin test.

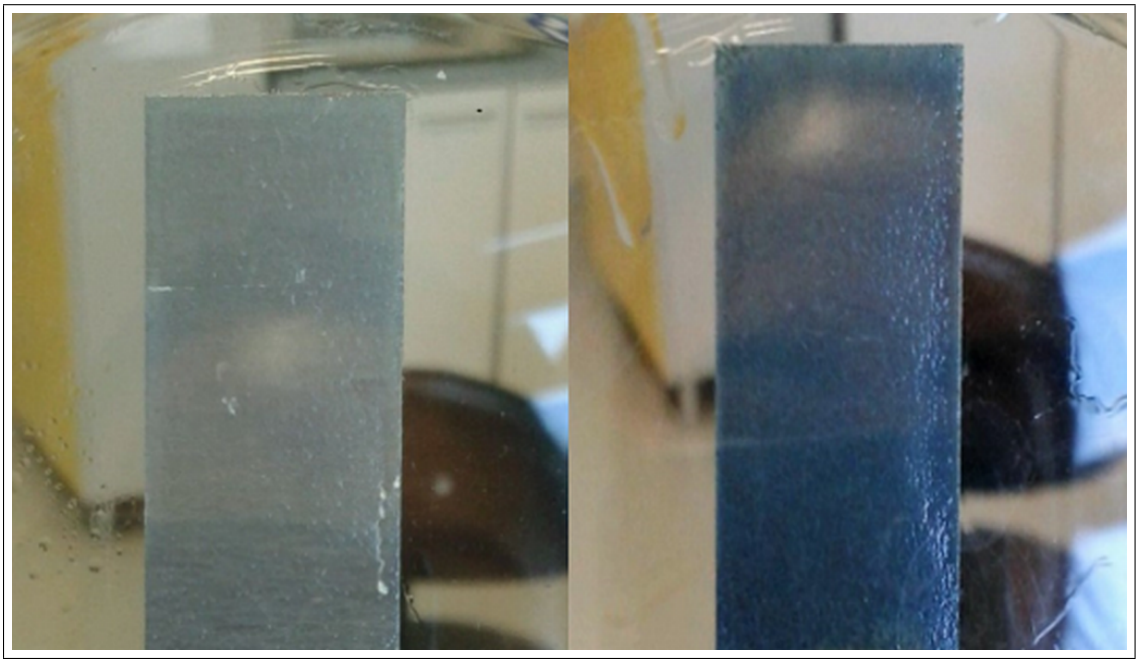

Figure 4.10 (a) HA coating after ninhydrin test (b) L-Arg/HA coating after ninhydrin test

As presented in Figure 4.10, there was no color change on HA coating but L-Arg/HA coating uniformly stained purple.

5. DISCUSSION

Ti6Al4V substrates which were magnetron sputtered with ZrO_2 were coated with HA via EPD and then L-Arg was self-assembled on HA coatings for the first time in the literature. Surface morphology and chemistry of the coatings. To confirm self-assembly of L-Arg on HA surface, SEM, FTIR, XPS and ninhydrin tests were carried out. The results of these tests were then compared with similar studies in the literature.

ZrO_2 coatings do not adhere easily on the smooth Ti6Al4V surface. Many studies roughened substrates by acid etching or sand-blasting before the coating process in order to increase coating adhesion and according to the study of Man et al. [111], adhesion strength of the coatings increased with the increase of the roughness [66, 87]. The smooth topography of Ti6Al4V implants transformed into a rough topography with nano-level changes after etching in HCl:distilled water:H_2SO_4 solution for 4 hours. Measurements taken by the profilometer showed an increase of the surface roughness from 0.04 μ to over 4 μ.

Raman spectrum of reactively sputtered ZrO_2 demonstrates the bands corresponding to monoclinic ZrO_2. Monoclinic ZrO_2 has strong lines at 180 cm^{-1}, 192 cm^{-1}, 476 cm^{-1} and weak lines at 223 cm^{-1}, 307 cm^{-1}, 502 cm^{-1}, 538 cm^{-1}, 559 cm^{-1}. It also has medium lines at 337 cm^{-1}, 348 cm^{-1}, 382 cm^{-1}, 617 cm^{-1} and 638 cm^{-1} [100, 101]. In Raman spectrum of reactively sputtered ZrO_2, Raman bands can be observed at 181 cm^{-1}, 189 cm^{-1}, 333 cm^{-1}, 380 cm^{-1}, 477 cm^{-1}, 555 cm^{-1} and 621 cm^{-1}. The small peaks at 220 cm^{-1} and 306 cm^{-1} can also be seen; however, Ti6Al4V substrate has a broad peak between 150 cm^{-1} and 350 cm^{-1}. Therefore, the bands at 220 cm^{-1} and 306 cm^{-1} are not so clear.

Raman analysis is not sufficient to determine the crystal structure of ZrO_2 since the band at 621 cm^{-1} corresponds to both monoclinic and tetragonal phases [101]. Therefore; to validate the results of the Raman analysis, XRD study was performed.

Figure 4.5 shows the XRD spectrum of ZrO_2 coating. According to XRD analysis, the peaks of monoclinic structure were present and no peak related to tetragonal phase was observed. Detailed scanning on software also proved that there was no tetragonal phase in the obtained ZrO_2 coating. This spectrum is provided in Appendix A. Moreover, the peaks of Ti6Al4V substrates are more intense than the peaks of ZrO_2 coating. Then, some bands could only be detected by the software (Appendix A). The relatively lower intensity of ZrO_2 peaks was correlated to ZrO_2 coating being too thin. This fact can be attributed to the thickness of the film. The obtained coating was a thin film which had a thickness of 240 nm. By reactive magnetron sputtering, thin films are produced unless the deposition rate is increased by adjusting the number and position of magnetrons [112].

After deposition of nano-sized ZrO_2 on Ti6Al4V, HA was coated with EPD. This technique enables production of homogeneous and porous coatings which lead to improved biological activity and fixation of the implant [88, 113, 114]. HA particles have strong tendency to agglomeration [115]. Using the suspensions with coagulated particles causes inhomogeneous coating layers and this leads to generation of cracks during sintering because of different shrinkage behavior of diverse species within the coating layer. Hence, preventing agglomeration of the particles is necessary [116]. Figure 4.5 shows uniform, crack-free, homogeneous and porous HA deposited with EPD. To prepare high-quality coatings, firstly, highly stable suspensions have to be prepared. Preparing HA suspensions in isopropanol without dispersant provided high suspension stability. Dispersants are usually suggested in order to prevent agglomeration of HA particles; however, such additives may cause contamination [115]. The advantage of selection of an organic medium for suspension stability is also recorded in many studies since the utilization of aqueous suspensions may cause local instability due to the gas evolution sourced from the electrolysis of water at low voltages [86, 115, 117, 118].

Ethanol and isopropanol are the mostly studied organic mediums for preparing HA suspensions [87, 88, 119]. Figure 4.5 shows that HA coatings with a dense microstructure is favorable to achieve high adhesion strength. Similar images can be seen in the study of Farrokhi-Rad et al.[120] who utilized isopropanol as a suspension

medium. According to the study of Farrokhi-Rad et al., dense and high-quality HA coatings can be obtained from HA suspension in isopropanol rather than ethanol. In optimization experiments of the study, the HA coatings produced from the suspension with ethanol were much thicker than the HA coatings produced from the suspension with isopropanol when voltage, duration and concentration were kept constant as 30 V, 1 minute and 1 g/35 ml, respectively. Similarly, Farrokhi et al. observed a higher deposition rate of HA particles in ethanol. Since HA particles in isopropanol have a higher zeta potential and a lower deposition rate, the particles are not prone to agglomerate and they can find enough time to homogeneously distribute on the substrate surface. A higher zeta potential and lower deposition rate are associated with the greater molecular size of isopropanol. The ionization reaction of the pure alcohol is as follows [121]:

$$RCH_2OH + RCH_2OH \longrightarrow RCH_2OH_2^+ + RCH_2O^-$$

The solubility of $RCH_2OH_2^+$ ions decrease with the increase of the molecular size of alcohol. This enhances the tendency of $RCH_2OH_2^+$ ions to adsorb on HA molecules by hydrogen bonding. Since the mobility of $RCH_2OH_2^+$[HA] particles is less than the mobility of $RCH_2OH_2^+$ species, the conductivity of HA suspension with isopropanol is lower than HA suspension with ethanol. This leads to a lower deposition rate and therefore, denser and higher-quality coatings can be produced [120].

As can be observed in XRD spectrum of HA-coated substrates, HA is the only calcium phosphate present in the coating. This means that sintering at 600 °C did not cause the decomposition of HA. This result is in correlation with the results in the literature. Many studies indicated that approximately 600 °C is efficient for the sintering process and this heat treatment profile also do not cause decomposition of HA [97, 116, 81].

Ninhydrin staining and SEM micrographs of L-Arg/HA coatings demonstrate the bound L-Arg molecules on HA layer. SEM micrographs of L-Arg/HA coatings which are illustrated in Figure 4.7 reveal the agglomeration of self-assembled L-Arg molecules on HA layer. Single nanoparticles of L-Arg are not distinct on SEM micrographs. This may be due to the similar structure of L-Arg particles to HA particles [122]. On the other hand, C1s spectrum of L-Arg/HA coatings exposed the new peaks at 285.74 eV and 288.69 eV which demonstrated the existence of the amino acid on the surface of HA [110]. For analysis of C1s spectrums, various studies based on HA, proteins, L-Arg/HA and protein/HA were investigated. According to these previous studies, carbon contamination is quite common for HA coatings [107] - [109]. The peak at 284.37 eV on the spectrum of HA coating and the peak at 284.48 eV on the spectrum of L-Arg/HA coating both refer to C-C bond. The increase in the intensity of this peak is associated with the increase in the amount of carbon with the addition of L-Arg [110].

In addition to the C1s spectrums, the change in the atomic percentages of elements reveals the changes in the chemical compositions on HA layer. These results were similar to the results of Jahromi et al. [16]. First, C/Ca ratio almost doubled up by the incorporation of L-Arg to HA due to the carbon containing groups of L-Arg. Second, the Ca/P ratio decreased. These results are associated with the incorporation of the carbon groups on HA surface. The FTIR spectrum also reveals the protonated carboxyl group. Therefore, it can be concluded that carboxyl groups of L-Arg particles bound to calcium atoms of HA particles as many previous studies stated [16, 123].

In conclusion, L-Arg/HA coatings on ZrO_2-coated Ti6Al4V implants were successfully prepared by self-assembly technique based on the results of SEM, FTIR, XPS analyses and ninhydrin staining. SEM micrographs showed agglomerated L-Arg particles which were self-assembled on HA layer. FTIR and XPS analyses revealed the increase of carbon content and the new bonds of C-O/N and O-C=O with the addition of L-Arg. Ninhydrin test also proved the existence of free amine groups on HA surface. XPS analyses also demonstrated the decrease of Ca/P and the increase of C/Ca, exposing the incorporation of carbon groups on HA structure. According to FTIR and

XPS results, L-Arg/HA coatings were obtained by the bond between the carboxyl of L-Arg and Ca atoms of HA. Overall, this thesis shows that self-assembly technique is a practical technique in order to produce L-Arg/HA coatings which have great potential for biomedical applications.

5.1 Future Studies

This study introduces self-assembly method in order to deposit L-Arg molecules on HA coatings which has a potential to increase osseointegration of HA coatings. The promising results may enlighten the future studies on orthopedic implants and bone tissue engineering. Currently, human bone marrow derived mesenchymal stem cells are subcultured till third passage. Alamar Blue test and alkaline phosphatase test will be performed in order to evaluate the effect of L-Arg on viability and differentiation of human bone marrow derived mesenchymal stem cells, respectively. In the future, in vivo studies may be performed to analyze the true potential of these implants for commercial applications.

APPENDIX A. SCAN ON XRD SOFTWARE

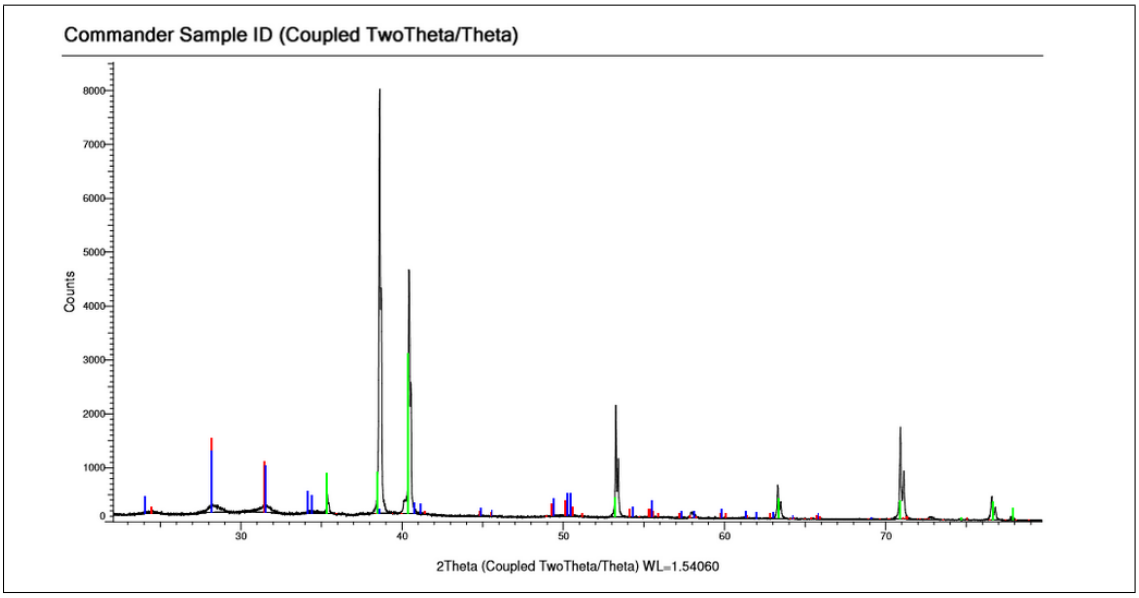

Figure A.1 Software scan of ZrO_2 coating (Blue lines: monoclinic phase, Green lines: substrate, Red lines: Undetected tetragonal phase)

APPENDIX B. Subculturing

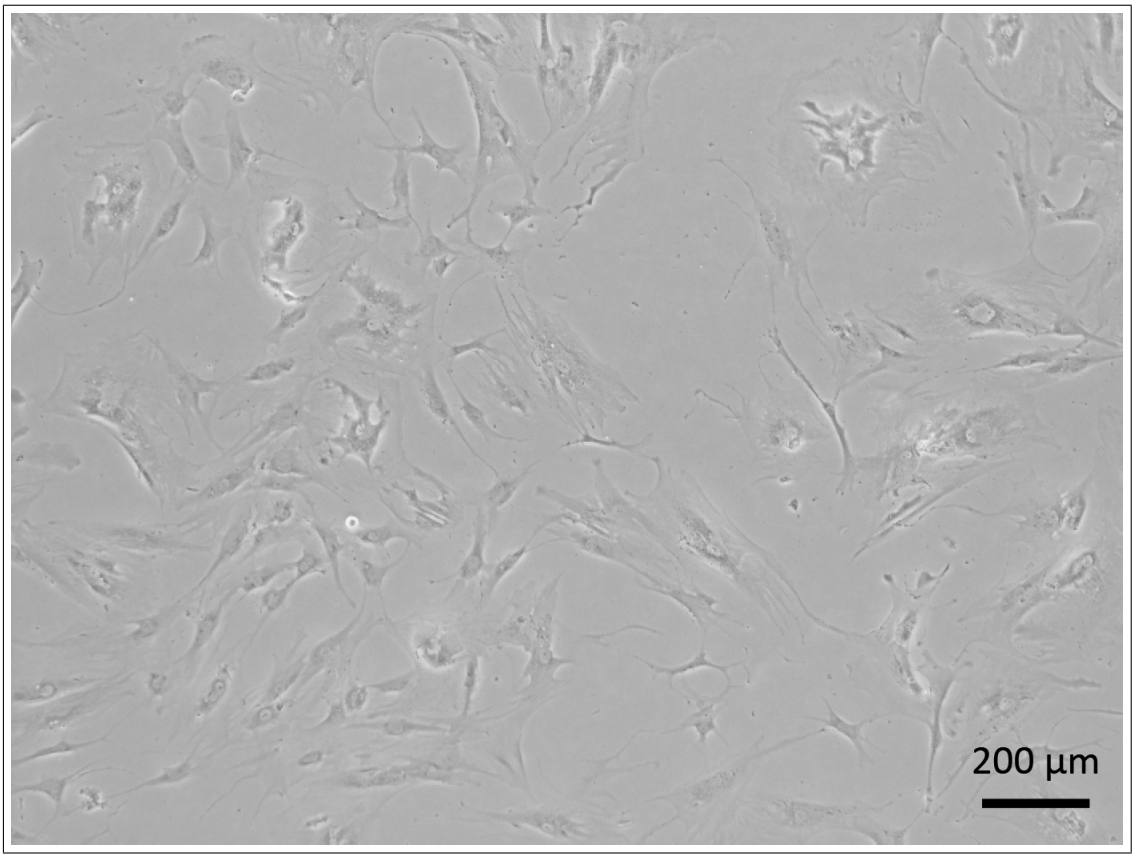

Figure B.1 Confluent human bone marrow mesenchymal stem cells at passage 2

REFERENCES

1. Rafieerad, A., M. Ashra, R. Mahmoodian, and A. Bushroa, "Surface characterization and corrosion behavior of calcium phosphate-base composite layer on titanium and its alloys via plasma electrolytic oxidation: A review paper," *Materials Science and Engineering: C*, Vol. 57, pp. 397–413, 2015.

2. Zhang, W., X. Chen, X. Liao, Z. Huang, X. Dan, and G. Yin, "Electrophoretic deposition of porous CaO–MgO–SiO_2 glass–ceramic coatings with B_2O_3 as additive on Ti–6Al–4V alloy," *Journal of Materials Science: Materials in Medicine*, Vol. 22, no. 10, p. 2261, 2011.

3. Sonntag, R., J. Reinders, J. Gibmeier, and J. P. Kretzer, "Fatigue performance of medical Ti6Al4V alloy after mechanical surface treatments," *PloS One*, Vol. 10, no. 3, p. e0121963, 2015.

4. Yadroitsev, I., P. Krakhmalev, and I. Yadroitsava, "Selective laser melting of ti6al4v alloy for biomedical applications: Temperature monitoring and microstructural evolution," *Journal of Alloys and Compounds*, Vol. 583, pp. 404–409, 2014.

5. Ege, D., İ. Duru, A. R. Kamali, and A. R. Boccaccini, "Nitride, zirconia, alumina, and carbide coatings on Ti6Al4V femoral heads: Effect of deposition techniques on mechanical and tribological properties," *Advanced Engineering Materials*, 2017.

6. Nishiguchi, S., H. Kato, H. Fujita, M. Oka, H.-M. Kim, T. Kokubo, and T. Nakamura, "Titanium metals form direct bonding to bone after alkali and heat treatments," *Biomaterials*, Vol. 22, no. 18, pp. 2525–2533, 2001.

7. Tsiourvas, D., A. Tsetsekou, M. Arkas, S. Diplas, and E. Mastrogianni, "Covalent attachment of a bioactive hyperbranched polymeric layer to titanium surface for the biomimetic growth of calcium phosphates," *Journal of Materials Science: Materials in Medicine*, Vol. 22, no. 1, pp. 85–96, 2011.

8. Xie, Y., J. Li, Z. Yu, and Q. Wei, "Nano modified sla process for titanium implants," *Materials Letters*, Vol. 186, pp. 38–41, 2017.

9. Lee, J. S., D. Suarez-Gonzalez, and W. L. Murphy, "Mineral coatings for temporally controlled delivery of multiple proteins," *Advanced Materials*, Vol. 23, no. 37, pp. 4279–4284, 2011.

10. Morra, M., "Biochemical modification of titanium surfaces: peptides and ecm proteins," *European Cells and Materials*, Vol. 12, no. 1, p. 15, 2006.

11. Gonzalez-McQuire, R., and A. Tsetsekou, "Hydroxyapatite-biomolecule coatings onto titanium surfaces," *Surface and Coatings Technology*, Vol. 203, no. 1, pp. 186–190, 2008.

12. Vater, C., A. Lode, A. Bernhardt, A. Reinstorf, B. Nies, and M. Gelinsky, "Modifications of a calcium phosphate cement with biomoleculesâinfluence on nanostructure, material, and biological properties," *Journal of Biomedical Materials Research Part A*, Vol. 95, no. 3, pp. 912–923, 2010.

13. He, J., T. Huang, L. Gan, Z. Zhou, B. Jiang, Y. Wu, F. Wu, and Z. Gu, "Collagen-infiltrated porous hydroxyapatite coating and its osteogenic properties: In vitro and in vivo study," *Journal of Biomedical Materials Research Part A*, Vol. 100, no. 7, pp. 1706–1715, 2012.

14. Bitschnau, A., V. Alt, F. Böhner, K. E. Heerich, E. Margesin, S. Hartmann, A. Sewing, C. Meyer, S. Wenisch, and R. Schnettler, "Comparison of new bone formation, implant integration, and biocompatibility between rgd-hydroxyapatite and pure hydroxyapatite coating for cementless joint prosthesesâan experimental study in rabbits," *Journal of Biomedical Materials Research Part B: Applied Biomaterials*, Vol. 88, no. 1, pp. 66–74, 2009.

15. Brigaud, I., R. Agniel, J. Leroy-Dudal, S. Kellouche, A. Ponche, T. Bouceba, N. Mihailescu, M. Sopronyi, E. Viguier, C. Ristoscu, *et al.*, "Synergistic effects of BMP-2, BMP-6 or BMP-7 with human plasma fibronectin onto hydroxyapatite coatings: A comparative study," *Acta Biomaterialia*, Vol. 55, pp. 481–492, 2017.

16. Jahromi, M. T., G. Yao, and M. Cerruti, "The importance of amino acid interactions in the crystallization of hydroxyapatite," *Journal of The Royal Society Interface*, Vol. 10, no. 80, p. 20120906, 2013.

17. Kim J W, Closs E I, A. L. M. C. J. M., "Transport of cationic amino acids by the mouse ecotropic retrovirus receptor," *Nature*, Vol. 352, no. 6337, pp. 725–728, 1991.

18. Lee, W.-H., C.-Y. Loo, K. L. Van, A. V. Zavgorodniy, and R. Rohanizadeh, "Modulating protein adsorption onto hydroxyapatite particles using different amino acid treatments," *Journal of The Royal Society Interface*, Vol. 9, no. 70, pp. 918–927, 2012.

19. Huh, J.-E., J.-Y. Choi, Y.-O. Shin, D.-S. Park, J. W. Kang, D. Nam, D.-Y. Choi, and J.-D. Lee, "Arginine enhances osteoblastogenesis and inhibits adipogenesis through the regulation of wnt and nfatc signaling in human mesenchymal stem cells," *International Journal of Molecular Sciences*, Vol. 15, no. 7, pp. 13010–13029, 2014.

20. Porter, J. R., T. T. Ruckh, and K. C. Popat, "Bone tissue engineering: a review in bone biomimetics and drug delivery strategies," *Biotechnology Progress*, Vol. 25, no. 6, pp. 1539–1560, 2009.

21. Wehrli, F. W., "Structural and functional assessment of trabecular and cortical bone by micro magnetic resonance imaging," *Journal of Magnetic Resonance Imaging*, Vol. 25, no. 2, pp. 390–409, 2007.

22. Rodan, G. A., "Bone homeostasis," *Proceedings of the National Academy of Sciences*, Vol. 95, no. 23, pp. 13361–13362, 1998.

23. Rho, J.-Y., L. Kuhn-Spearing, and P. Zioupos, "Mechanical properties and the hierarchical structure of bone," *Medical Engineering & Physics*, Vol. 20, no. 2, pp. 92–102, 1998.

24. Weiner, S., and H. D. Wagner, "The material bone: structure-mechanical function relations," *Annual Review of Materials Science*, Vol. 28, no. 1, pp. 271–298, 1998.

25. Long, F., "Building strong bones: molecular regulation of the osteoblast lineage," *Nature Reviews. Molecular Cell Biology*, Vol. 13, no. 1, p. 27, 2012.

26. Downey, P. A., and M. I. Siegel, "Bone biology and the clinical implications for osteoporosis," *Physical Therapy*, Vol. 86, no. 1, pp. 77–91, 2006.

27. Mendelson, A., and P. S. Frenette, "Hematopoietic stem cell niche maintenance during homeostasis and regeneration," *Nature Medicine*, Vol. 20, no. 8, pp. 833–846, 2014.

28. Cosman, F., S. De Beur, M. LeBoff, E. Lewiecki, B. Tanner, S. Randall, and R. Lindsay, "Clinicianâs guide to prevention and treatment of osteoporosis," *Osteoporosis International*, Vol. 25, no. 10, pp. 2359–2381, 2014.

29. Dempster, D. W., E. Shane, W. Horbert, and R. Lindsay, "A simple method for correlative light and scanning electron microscopy of human iliac crest bone biopsies: qualitative observations in normal and osteoporotic subjects," *Journal of Bone and Mineral Research*, Vol. 1, no. 1, pp. 15–21, 1986.

30. Hayami, T., M. Pickarski, G. A. Wesolowski, J. Mclane, A. Bone, J. Destefano, G. A. Rodan, and L. T. Duong, "The role of subchondral bone remodeling in osteoarthritis: reduction of cartilage degeneration and prevention of osteophyte formation by alendronate in the rat anterior cruciate ligament transection model," *Arthritis & Rheumatology*, Vol. 50, no. 4, pp. 1193–1206, 2004.

31. Liu, Y., J. Wu, Y. Zhu, and J. Han, "Therapeutic application of mesenchymal stem cells in bone and joint diseases," *Clinical and Experimental Medicine*, Vol. 14, no. 1, pp. 13–24, 2014.

32. Panisello, J. J., L. Herrero, V. Canales, A. Herrera, A. A. Martínez, and J. Mateo, "Long-term remodeling in proximal femur around a hydroxyapatite-coated anatomic stem: ten years densitometric follow-up," *The Journal of Arthroplasty*, Vol. 24, no. 1, pp. 56–64, 2009.

33. Prevoo, M., M. Van't Hof, H. Kuper, M. Van Leeuwen, L. Van De Putte, and P. Van Riel, "Modified disease activity scores that include twenty-eight-joint counts development and validation in a prospective longitudinal study of patients with rheumatoid arthritis," *Arthritis & Rheumatology*, Vol. 38, no. 1, pp. 44–48, 1995.

34. Parekh, R., R. Dwek, B. Sutton, D. Fernandes, A. Leung, D. Stanworth, T. Rademacher, T. Mizuochi, T. Taniguchi, K. Matsuta, *et al.*, "Association of rheumatoid arthritis and primary osteoarthritis with changes in the glycosylation pattern of total serum igg," *Nature*, Vol. 316, no. 6027, pp. 452–457, 1985.

35. Walter, G., M. Vernier, P. Pinelli, M. Million, M. Coulange, P. Seng, and A. Stein, "Bone and joint infections due to anaerobic bacteria: an analysis of 61 cases and review of the literature," *European Journal of Clinical Microbiology & Infectious Diseases*, Vol. 33, no. 8, pp. 1355–1364, 2014.

36. Puckett, S., R. Pareta, and T. J. Webster, "Nano rough micron patterned titanium for directing osteoblast morphology and adhesion," *International Journal of Nanomedicine*, Vol. 3, no. 2, pp. 229–241, 2008.

37. Gilbert, J. L., C. A. Buckley, and J. J. Jacobs, "In vivo corrosion of modular hip prosthesis components in mixed and similar metal combinations. the effect of crevice, stress, motion, and alloy coupling," *Journal of Biomedical Materials Research Part A*, Vol. 27, no. 12, pp. 1533–1544, 1993.

38. Geesink, R. G., K. De Groot, and C. P. Klein, "Chemical implant fixation using hydroxyl-apatite coatings: The development of a human total hip prosthesis for chemical fixation to bone using hydroxyl-apatite coatings on titanium substrates.," *Clinical Orthopaedics and Related Research*, Vol. 225, pp. 147–170, 1987.

39. Tauber, C., H. B. Itzhak, and C. Malkin, "Bone grafting in total hip replacement for acetabular protrusion: A review of 11 operations," *Acta Orthopaedica Scandinavica*, Vol. 55, no. 5, pp. 507–509, 1984.

40. Katz, J. N., "Total joint replacement in osteoarthritis," *Best Practice & Research Clinical Rheumatology*, Vol. 20, no. 1, pp. 145–153, 2006.

41. Rodriguez, J. A., S. Saddler, S. Edelman, and C. S. Ranawat, "Long-term results of total knee arthroplasty in class 3 and 4 rheumatoid arthritis," *The Journal of Arthroplasty*, Vol. 11, no. 2, pp. 141–145, 1996.

42. Liu, X., P. K. Chu, and C. Ding, "Surface modification of titanium, titanium alloys, and related materials for biomedical applications," *Materials Science and Engineering: R: Reports*, Vol. 47, no. 3, pp. 49–121, 2004.

43. Raphel, J., M. Holodniy, S. B. Goodman, and S. C. Heilshorn, "Multifunctional coatings to simultaneously promote osseointegration and prevent infection of orthopaedic implants," *Biomaterials*, Vol. 84, pp. 301–314, 2016.

44. Anissian, H. L., A. Stark, A. Gustafson, V. Good, and I. C. Clarke, "Metal-on-metal bearing in hip prosthesis generates 100-fold less wear debris than metal-on-polyethylene," *Acta Orthopaedica Scandinavica*, Vol. 70, no. 6, pp. 578–582, 1999.

45. Sharkey, P. F., W. J. Hozack, R. H. Rothman, S. Shastri, and S. M. Jacoby, "Why are total knee arthroplasties failing today?," *Clinical Orthopaedics and Related Research*, Vol. 404, pp. 7–13, 2002.

46. Trampuz, A., and A. F. Widmer, "Infections associated with orthopedic implants," *Current Opinion in Infectious Diseases*, Vol. 19, no. 4, pp. 349–356, 2006.

47. Schrama, J. C., B. Espehaug, G. Hallan, L. B. Engesæter, O. Furnes, L. I. Havelin, and B.-T. S. Fevang, "Risk of revision for infection in primary total hip and knee arthroplasty in patients with rheumatoid arthritis compared with osteoarthritis: A prospective, population-based study on 108,786 hip and knee joint arthroplasties from the norwegian arthroplasty register," *Arthritis Care & Research*, Vol. 62, no. 4, pp. 473–479, 2010.

48. Park, K.-H., K. E. Greenwood-Quaintance, A. D. Hanssen, M. P. Abdel, and R. Patel, "Antimicrobial-loaded bone cement does not negatively influence sonicate fluid culture positivity for the diagnosis of prosthetic joint infection," *Journal of Clinical Microbiology*, pp. 1–11, 2016.

49. Man, H., M. Bai, and F. Cheng, "Laser diffusion nitriding of ti–6al–4v for improving hardness and wear resistance," *Applied Surface Science*, Vol. 258, no. 1, pp. 436–441, 2011.

50. Wang, G., and H. Zreiqat, "Functional coatings or films for hard-tissue applications," *Materials*, Vol. 3, no. 7, pp. 3994–4050, 2010.

51. Bedi, R. S., D. E. Beving, L. P. Zanello, and Y. Yan, "Biocompatibility of corrosion-resistant zeolite coatings for titanium alloy biomedical implants," *Acta Biomaterialia*, Vol. 5, no. 8, pp. 3265–3271, 2009.

52. Banerjee, R., S. Nag, and H. Fraser, "A novel combinatorial approach to the development of beta titanium alloys for orthopaedic implants," *Materials Science and Engineering: C*, Vol. 25, no. 3, pp. 282–289, 2005.

53. Drnovšek, N., S. Novak, U. Dragin, M. Čeh, M. Gorenšek, and M. Gradišar, "Bioactive glass enhances bone ingrowth into the porous titanium coating on orthopaedic implants," *International Orthopaedics*, Vol. 36, no. 8, pp. 1739–1745, 2012.

54. Cannillo, V., J. Colmenares-Angulo, L. Lusvarghi, F. Pierli, and S. Sampath, "In vitro characterisation of plasma-sprayed apatite/wollastonite glass–ceramic biocoatings on titanium alloys," *Journal of the European Ceramic Society*, Vol. 29, no. 9, pp. 1665–1677, 2009.

55. Hübsch, C., P. Dellinger, H. Maier, F. Stemme, M. Bruns, M. Stiesch, and L. Borchers, "Protection of yttria-stabilized zirconia for dental applications by oxidic pvd coating," *Acta Biomaterialia*, Vol. 11, pp. 488–493, 2015.

56. Carinci, F., F. Pezzetti, S. Volinia, F. Francioso, D. Arcelli, E. Farina, and A. Piattelli, "Zirconium oxide: analysis of mg63 osteoblast-like cell response by means of a microarray technology," *Biomaterials*, Vol. 25, no. 2, pp. 215–228, 2004.

57. Leib, E. W., R. M. Pasquarelli, J. J. do Rosário, P. N. Dyachenko, S. Döring, A. Puchert, A. Y. Petrov, M. Eich, G. A. Schneider, R. Janssen, *et al.*, "Yttria-stabilized zirconia microspheres: novel building blocks for high-temperature photonics," *Journal of Materials Chemistry C*, Vol. 4, no. 1, pp. 62–74, 2016.

58. Manicone, P. F., P. R. Iommetti, and L. Raffaelli, "An overview of zirconia ceramics: basic properties and clinical applications," *Journal of Dentistry*, Vol. 35, no. 11, pp. 819–826, 2007.

59. Garvie, R. C., "The occurrence of metastable tetragonal zirconia as a crystallite size effect," *The Journal of Physical Chemistry*, Vol. 69, no. 4, pp. 1238–1243, 1965.

60. Garvie, R., "Stabilization of the tetragonal structure in zirconia microcrystals," *The Journal of Physical Chemistry*, Vol. 82, no. 2, pp. 218–224, 1978.

61. Nogiwa-Valdez, A., W. Rainforth, and T. Stewart, "Wear and degradation on retrieved zirconia femoral heads," *Journal of the Mechanical Behavior of Biomedical Materials*, Vol. 31, pp. 145–151, 2014.

62. Wang, G., F. Meng, C. Ding, P. K. Chu, and X. Liu, "Microstructure, bioactivity and osteoblast behavior of monoclinic zirconia coating with nanostructured surface," *Acta Biomaterialia*, Vol. 6, no. 3, pp. 990–1000, 2010.

63. Chevalier, J., L. Gremillard, A. V. Virkar, and D. R. Clarke, "The tetragonal-monoclinic transformation in zirconia: lessons learned and future trends," *Journal of the American Ceramic Society*, Vol. 92, no. 9, pp. 1901–1920, 2009.

64. Haraguchi, K., N. Sugano, T. Nishii, H. Miki, K. Oka, and H. Yoshikawa, "Phase transformation of a zirconia ceramic head after total hip arthroplasty," *Bone & Joint Journal*, Vol. 83, no. 7, pp. 996–1000, 2001.

65. Braun, R., K. Kelm, M. Fröhlich, and C. Leyens, "Oxidation resistance of γ-tial based alloy ti–45al–8nb coated with intermetallic ti–al–cr–y layers and eb-pvd zirconia topcoats at 950Â° c in air," *Surface and Coatings Technology*, Vol. 222, pp. 128–134, 2013.

66. Zhao, Y., Z. Zhang, Q. Dai, D. Lin, and S. Li, "Microstructure and bond strength of ha (+ zro 2+ y 2 o 3)/ti6al4v composite coatings fabricated by rf magnetron sputtering," *Surface and Coatings Technology*, Vol. 200, no. 18, pp. 5354–5363, 2006.

67. Guo, L., J. Zhao, X. Wang, X. Xu, H. Liu, and Y. Li, "Structure and bioactivity of zirconia nanotube arrays fabricated by anodization," *International Journal of Applied Ceramic Technology*, Vol. 6, no. 5, pp. 636–641, 2009.

68. Yan, Y., and Y. Han, "Structure and bioactivity of micro-arc oxidized zirconia films," *Surface and Coatings Technology*, Vol. 201, no. 9, pp. 5692–5695, 2007.

69. Maleki-Ghaleh, H., M. Rekabeslami, M. Shakeri, M. Siadati, M. Javidi, S. Talebian, and H. Aghajani, "Nano-structured yttria-stabilized zirconia coating by electrophoretic deposition," *Applied Surface Science*, Vol. 280, pp. 666–672, 2013.

70. Kelly, P., and R. Arnell, "Magnetron sputtering: a review of recent developments and applications," *Vacuum*, Vol. 56, no. 3, pp. 159–172, 2000.

71. Pessoa, R., M. Fraga, L. Santos, N. Galvão, H. Maciel, and M. Massi, "Plasma-assisted techniques for growing hard nanostructured coatings: an overview," *Anti-Abrasive Nanocoatings: Current and Future Applications*, pp. 455–479, 2014.

72. Salinas, A. J., and M. Vallet-Regí, "Bioactive ceramics: from bone grafts to tissue engineering," *RSC Advances*, Vol. 3, no. 28, pp. 11116–11131, 2013.

73. Chao, C.-S., K.-H. Liu, W.-L. Tung, S.-Y. Chen, D.-M. Liu, and Y.-P. Chang, "Bioactive tio2 ultrathin film with worm-like mesoporosity for controlled drug delivery," *Microporous and Mesoporous Materials*, Vol. 152, pp. 58–63, 2012.

74. Mohseni, E., E. Zalnezhad, and A. R. Bushroa, "Comparative investigation on the adhesion of hydroxyapatite coating on ti–6al–4v implant: A review paper," *International Journal of Adhesion and Adhesives*, Vol. 48, pp. 238–257, 2014.

75. Palazzo, B., D. Walsh, M. Iafisco, E. Foresti, L. Bertinetti, G. Martra, C. L. Bianchi, G. Cappelletti, and N. Roveri, "Amino acid synergetic effect on structure, morphology and surface properties of biomimetic apatite nanocrystals," *Acta Biomaterialia*, Vol. 5, no. 4, pp. 1241–1252, 2009.

76. Qiu, Z., G. Li, Y. Zhang, J. Liu, W. Hu, J. Ma, and S. Zhang, "Fine structure analysis and sintering properties of si-doped hydroxyapatite," *Biomedical Materials*, Vol. 7, no. 4, p. 045009, 2012.

77. Fu, L., K. A. Khor, and J. P. Lim, "Effects of yttria-stabilized zirconia on plasma-sprayed hydroxyapatite/yttria-stabilized zirconia composite coatings," *Journal of the American Ceramic Society*, Vol. 85, no. 4, pp. 800–806, 2002.

78. Khalid, M., M. Mujahid, A. N. Khan, and R. Rawat, "Dip coating of nano hydroxyapatite on titanium alloy with plasma assisted γ-alumina buffer layer: a novel coating approach," *Journal of Materials Science & Technology*, Vol. 29, no. 6, pp. 557–564, 2013.

79. McManamon, C., J. P. de Silva, J. Power, S. Ramirez-Garcia, M. A. Morris, and G. L. Cross, "Interfacial characteristics and determination of cohesive and adhesive strength of plasma-coated hydroxyapatite via nanoindentation and microscratch techniques," *Langmuir*, Vol. 30, no. 38, pp. 11412–11420, 2014.

80. Biasetto, L., H. Elsayed, F. Bonollo, and P. Colombo, "Polymer-derived sphene biocoating on cp-ti substrates for orthopedic and dental implants," *Surface and Coatings Technology*, Vol. 301, pp. 140–147, 2016.

81. Khor, K., Y. Gu, D. Pan, and P. Cheang, "Microstructure and mechanical properties of plasma sprayed ha/ysz/ti–6al–4v composite coatings," *Biomaterials*, Vol. 25, no. 18, pp. 4009–4017, 2004.

82. Kong, D.-j., L. Dan, Y.-z. Wu, and C.-z. Zhou, "Mechanical properties of hydroxyapatite-zirconia coatings prepared by magnetron sputtering," *Transactions of Nonferrous Metals Society of China*, Vol. 22, no. 1, pp. 104–110, 2012.

83. Mavis, B., and A. C. Taş, "Dip coating of calcium hydroxyapatite on Ti-6Al-4V substrates," *Journal of the American Ceramic Society*, Vol. 83, no. 4, pp. 989–991, 2000.

84. Sidane, D., D. Chicot, S. Yala, S. Ziani, H. Khireddine, A. Iost, and X. Decoopman, "Study of the mechanical behavior and corrosion resistance of hydroxyapatite sol–gel thin coatings on 316 L stainless steel pre-coated with titania film," *Thin Solid Films*, Vol. 593, pp. 71–80, 2015.

85. Salehi, A., H. A. Mashhadi, M. Abravi, and H. Jafarian, "An ultrasound-assisted method on the formation of nanocrystalline fluorohydroxyapatite coatings on titanium scaffold by dip coating process," *Procedia Materials Science*, Vol. 11, pp. 137–141, 2015.

86. Javidi, M., S. Javadpour, M. Bahrololoom, and J. Ma, "Electrophoretic deposition of natural hydroxyapatite on medical grade 316l stainless steel," *Materials Science and Engineering: C*, Vol. 28, no. 8, pp. 1509–1515, 2008.

87. Drevet, R., N. B. Jaber, J. Fauré, A. Tara, A. B. C. Larbi, and H. Benhayoune, "Electrophoretic deposition (EPD) of nano-hydroxyapatite coatings with improved mechanical properties on prosthetic ti6al4v substrates," *Surface and Coatings Technology*, Vol. 301, pp. 94–99, 2016.

88. Boccaccini, A., S. Keim, R. Ma, Y. Li, and I. Zhitomirsky, "Electrophoretic deposition of biomaterials," *Journal of the Royal Society Interface*, Vol. 7, no. Suppl 5, pp. 581–613, 2010.

89. Seuss, S., and A. R. Boccaccini, "Electrophoretic deposition of biological macromolecules, drugs, and cells," *Biomacromolecules*, Vol. 14, no. 10, pp. 3355–3369, 2013.

90. Corni, I., M. P. Ryan, and A. R. Boccaccini, "Electrophoretic deposition: from traditional ceramics to nanotechnology," *Journal of the European Ceramic Society*, Vol. 28, no. 7, pp. 1353–1367, 2008.

91. Brasinika, D., O. Tsigkou, A. Tsetsekou, and Y. F. Missirlis, "Bioinspired synthesis of hydroxyapatite nanocrystals in the presence of collagen and l-arginine: Candidates for bone regeneration," *Journal of Biomedical Materials Research Part B: Applied Biomaterials*, Vol. 104, no. 3, pp. 458–469, 2016.

92. Salick, D. A., D. J. Pochan, and J. P. Schneider, "Design of an injectable β-hairpin peptide hydrogel that kills methicillin-resistant staphylococcus aureus," *Advanced Materials*, Vol. 21, no. 41, pp. 4120–4123, 2009.

93. Chan, D. I., E. J. Prenner, and H. J. Vogel, "Tryptophan-and arginine-rich antimicrobial peptides: structures and mechanisms of action," *Biochimica et Biophysica Acta (BBA)-Biomembranes*, Vol. 1758, no. 9, pp. 1184–1202, 2006.

94. Shafer, W. M., F. Hubalek, M. Huang, and J. Pohl, "Bactericidal activity of a synthetic peptide (cg 117-136) of human lysosomal cathepsin g is dependent on arginine content.," *Infection and Immunity*, Vol. 64, no. 11, pp. 4842–4845, 1996.

95. Mertens, T., and H. Kollek, "On the stability and composition of oxide layers on pretreated titanium," *International Journal of Adhesion and Adhesives*, Vol. 30, no. 6, pp. 466–477, 2010.

96. Zhitomirsky, I., and L. Gal-Or, "Electrophoretic deposition of hydroxyapatite," *Journal of Materials Science: Materials in Medicine*, Vol. 8, no. 4, pp. 213–219, 1997.

97. Drdlik, D., M. Slama, H. Hadraba, K. Drdlikova, and J. Cihlar, "On the role of the indifferent electrolyte licl in electrophoretic deposition of hydroxyapatite from 2-propanol dispersions," *Ceramics International*, Vol. 42, no. 15, pp. 16529–16534, 2016.

98. Chuah, Y. J., Y. T. Koh, K. Lim, N. V. Menon, Y. Wu, and Y. Kang, "Simple surface engineering of polydimethylsiloxane with polydopamine for stabilized mesenchymal stem cell adhesion and multipotency," *Scientific Reports*, Vol. 5, no. 18162.

99. Kim, Y.-H., M. A. Jyoti, and H.-Y. Song, "Immobilization of cross linked col-i–opn bone matrix protein on aminolysed pcl surfaces enhances initial biocompatibility of human adipogenic mesenchymal stem cells (HADMSC)," *Applied Surface Science*, Vol. 303, pp. 97–106, 2014.

100. Rawat, M., A. Das, D. Shukla, P. Rajput, A. Chettah, D. Phase, R. Ramola, and F. Singh, "Micro-raman and electronic structure study on kinetics of electronic excitations induced monoclinic-to-tetragonal phase transition in zirconium oxide films," *RSC Advances*, Vol. 6, no. 106, pp. 104425–104432, 2016.

101. Phillippi, C., and K. Mazdiyasni, "Infrared and raman spectra of zirconia polymorphs," *Journal of the American Ceramic Society*, Vol. 54, no. 5, pp. 254–258, 1971.

102. Balakrishnan, K., A. Datar, T. Naddo, J. Huang, R. Oitker, M. Yen, J. Zhao, and L. Zang, "Effect of side-chain substituents on self-assembly of perylene diimide molecules: morphology control," *Journal of the American Chemical Society*, Vol. 128, no. 22, pp. 7390–7398, 2006.

103. Mandal, D., R. K. Tiwari, A. N. Shirazi, D. Oh, G. Ye, A. Banerjee, A. Yadav, and K. Parang, "Self-assembled surfactant cyclic peptide nanostructures as stabilizing agents," *Soft Matter*, Vol. 9, no. 39, pp. 9465–9475, 2013.

104. Wang, Z., L. Dong, L. Han, K. Wang, X. Lu, L. Fang, S. Qu, and C. W. Chan, "Self-assembled biodegradable nanoparticles and polysaccharides as biomimetic ecm nanostructures for the synergistic effect of RGD and BMP-2 on bone formation," *Scientific Reports*, Vol. 6, no. 25090, pp. 1–12.

105. Hendler, R. W., C. W. Meuse, M. S. Braiman, P. D. Smith, and J. W. Kakareka, "Infrared and visible absolute and difference spectra of bacteriorhodopsin photocycle intermediates," *Applied Spectroscopy*, Vol. 65, no. 9, pp. 1029–1045, 2011.

106. Puustinen, A., J. A. Bailey, R. B. Dyer, S. L. Mecklenburg, M. Wikström, and W. H. Woodruff, "Fourier transform infrared evidence for connectivity between cub and glutamic acid 286 in cytochrome bo 3 from escherichia coli," *Biochemistry*, Vol. 36, no. 43, pp. 13195–13200, 1997.

107. Gu, Y., K. Khor, and P. Cheang, "In vitro studies of plasma-sprayed hydroxyapatite/ti-6al-4v composite coatings in simulated body fluid (SBF)," *Biomaterials*, Vol. 24, no. 9, pp. 1603–1611, 2003.

108. Durrieu, M.-C., S. Pallu, F. Guillemot, R. Bareille, J. Amédée, C. Baquey, C. Labrugère, and M. Dard, "Grafting RGD containing peptides onto hydroxyapatite to promote osteoblastic cells adhesion," *Journal of Materials Science: Materials in Medicine*, Vol. 15, no. 7, pp. 779–786, 2004.

109. Boyd, A., G. Burke, H. Duffy, M. Holmberg, C. OâKane, B. Meenan, and P. Kingshott, "Sputter deposited bioceramic coatings: surface characterisation and initial protein adsorption studies using surface-MALDI-MS," *Journal of Materials Science: Materials in Medicine*, Vol. 22, no. 1, pp. 71–84, 2011.

110. Fang, J., I. Levchenko, A. Mai-Prochnow, M. Keidar, U. Cvelbar, G. Filipic, Z. J. Han, and K. K. Ostrikov, "Protein retention on plasma-treated hierarchical nanoscale gold-silver platform," *Scientific Reports*, Vol. 5, no. 13379, pp. 1–11, 2015.

111. Man, H., K. Chiu, F. Cheng, and K. Wong, "Adhesion study of pulsed laser deposited hydroxyapatite coating on laser surface nitrided titanium," *Thin Solid Films*, Vol. 517, no. 18, pp. 5496–5501, 2009.

112. Musil, J., P. Baroch, J. Vlček, K. Nam, and J. Han, "Reactive magnetron sputtering of thin films: present status and trends," *Thin Solid Films*, Vol. 475, no. 1, pp. 208–218, 2005.

113. Frajkorová, F., E. Molero, P. Montero, M. C. Gomez-Guillen, A. J. Sanchez-Herencia, and B. Ferrari, "Biodegradable bi-layered coatings shaped by dipping of Ti films followed by the EPD of gelatin/hydroxyapatite composites," *Journal of the European Ceramic Society*, Vol. 36, no. 2, pp. 343–355, 2016.

114. Zhang, H., J. Krajewski, Z. Zhang, M. Masopust, and D. T. Xiao, "Nano-hydroxyapatite coated femoral stem implant by electrophoretic deposition," *MRS Online Proceedings Library Archive*, Vol. 975, 2007.

115. Xiao, X. F., and R. F. Liu, "Effect of suspension stability on electrophoretic deposition of hydroxyapatite coatings," *Materials Letters*, Vol. 60, no. 21, pp. 2627–2632, 2006.

116. Kaya, C., "Electrophoretic deposition of carbon nanotube-reinforced hydroxyapatite bioactive layers on Ti–6Al–4V alloys for biomedical applications," *Ceramics International*, Vol. 34, no. 8, pp. 1843–1847, 2008.

117. Loghmani, S. K., M. Farrokhi-Rad, and T. Shahrabi, "Effect of polyethylene glycol on the electrophoretic deposition of hydroxyapatite nanoparticles in isopropanol," *Ceramics International*, Vol. 39, no. 6, pp. 7043–7051, 2013.

118. Besra, L., and M. Liu, "A review on fundamentals and applications of electrophoretic deposition (EPD)," *Progress in Materials Science*, Vol. 52, no. 1, pp. 1–61, 2007.

119. Ma, J., C. Liang, L. Kong, and C. Wang, "Colloidal characterization and electrophoretic deposition of hydroxyapatite on titanium substrate," *Journal of Materials Science: Materials in Medicine*, Vol. 14, no. 9, pp. 797–801, 2003.

120. Farrokhi-Rad, M., and T. Shahrabi, "Effect of suspension medium on the electrophoretic deposition of hydroxyapatite nanoparticles and properties of obtained coatings," *Ceramics International*, Vol. 40, no. 2, pp. 3031–3039, 2014.

121. Damodaran, R., and B. Moudgil, "Electrophoretic deposition of calcium phosphates from non-aqueous media," *Colloids and Surfaces A: Physicochemical and Engineering Aspects*, Vol. 80, no. 2, pp. 191–195, 1993.

122. Lakio, S., D. A. Morton, A. P. Ralph, and P. Lambert, "Optimizing aerosolization of a high-dose L-arginine powder for pulmonary delivery," *Asian Journal of Pharmaceutical Sciences*, Vol. 10, no. 6, pp. 528–540, 2015.

123. Sionkowska, A., and J. Kozłowska, "Properties and modification of porous 3-D collagen/hydroxyapatite composites," *International Journal of Biological Macromolecules*, Vol. 52, pp. 250–259, 2013.